Received: 9 October 2023 | Revised: 8 December 2023 | Accepted: 7 January 2024

DOI: 10.1002/nme.7433

RESEARCH ARTICLE

WILEY

A FE2 shell model with periodic boundary conditions for thin and thick shells

Friedrich Gruttmann[1] | **Werner Wagner**[2]

[1]Technische Universität Darmstadt, Institut für Mechanik, Darmstadt, Germany

[2]Karlsruher Institut für Technologie, Institut für Baustatik, Karlsruhe, Germany

Correspondence
Friedrich Gruttmann, Technische Universität Darmstadt, Institut für Mechanik, Franziska-Braun-Str. 7, 64287 Darmstadt, Germany.
Email: gruttmann@mechanik.tu-darmstadt.de

Abstract

In this article a FE2 shell model for thin and thick shells within a first order homogenization scheme is presented. A variational formulation for the two-scale boundary value problem and the associated finite element formulation is developed. Constraints with 5 or 9 Lagrange parameters are derived which eliminate both rigid body movements and dependencies of the shear stiffness on the size of the representative volume elements (RVEs). At the bottom and top surface of the RVEs which extend through the total thickness of the shell stress boundary conditions are present. The periodic boundary conditions at the lateral surfaces are applied in such a way that particular membrane, bending and shear modes are not restrained. This is shown by means of a homogeneous RVE. The first of all linear formulation is extended to finite strain problems introducing transformation relations for the stress resultants and the material matrix. The transformations are performed at the Gauss points on macro level. Several boundary value problems including large deformations, stability and inelasticity are computed and compared with 3D reference solutions.

KEYWORDS

FE2 shell modeling, homogeneous RVE as benchmark, inhomogeneous shell examples, periodic boundary conditions, Reissner–Mindlin theory

1 | INTRODUCTION

Heterogeneous plates and shells are used in many technical disciplines. As examples fiber reinforced composite sheets and panels are increasingly used in aerospace and automotive industries. The advantages of these structures are high stiffness and strength values along with low weight. The application of a so-called full-scale model that includes all fine scale details can quickly result in a large-scale simulation with an impractical number of degrees of freedom. So called bubble decks with thousands of spherical hollow bodies to save some weight is a plate example in civil engineering where a fine micro structure occurs. Thus, an explicit modeling of all heterogeneities is often not possible. To avoid such large-scale computations, the bodies are treated as a homogeneous continuum with effective properties obtained through a homogenization procedure. Continua with a heterogeneous microstructure that periodically repeats itself in small vicinities of the structure allow for the exploitation of the so-called scale separation condition. Arbitrary material behavior on the micro

This article is dedicated to Professor Robert L. Taylor on the occasion of his 90th birthday. We personally thank Bob for his close friendship over decades. The pioneering concept of FEAP is a valuable basis of our research and has led to numerous publications and doctoral theses in our groups.

level including physical and geometrical evolution of the microstructure can be considered. Solutions of two coupled boundary value problems, one on the macro scale and one on the micro scale, are computed. Computational homogenization methods are well suited for parallelization. The computing time to set up the global stiffness matrix is practically scaled by the number of processors.

A lot of literature exists on computational homogenization methods for general heterogeneous materials, see for example, References 1 and 2 for a survey. The theoretical framework of multi-scale modeling in continuum mechanics is well established, for example, References 3–10 among many others.

Sandwich panels consist of a heterogeneous core bonded to the face sheets. Effective properties of the core can first be determined applying analytical or numerical homogenization methods for a three-dimensional continuum. Hence the whole sandwich structure can be analyzed by application of a laminate theory, see for example, References 11–14. The homogenization of masonry structures considering a particular stacking and material behavior of the constituents has been treated for example, in References 15–18. Based on a second order computational homogenization approach[19] procedures for thin structured sheets have been proposed.[20,21] The theory in Reference 20 is based on a Reissner–Mindlin kinematic, whereas in Reference 21 a Kirchhoff-Love kinematic is adopted. Representative volume elements (RVE) extending through the total thickness of the structure are introduced. At the top and bottom surfaces of the RVE stress boundary conditions are applied, whereas periodicity constraints are applied at the lateral surfaces. The authors of Reference 22 develop general orthogonality conditions for second gradient multiscale homogenization of statistical volume elements. Numerical multiscale modeling of linear sandwich plates based on a Reissner–Mindlin plate theory with seven degrees of freedom have been developed to account for thickness change.[23] A stress–resultant shell theory based on two-scale homogenization is presented in Reference 24. The authors apply a first-order Taylor series expansion for the in-plane displacements, and a second-order expansion for the through-thickness normal components.

Nonlinear layered shells are considered in Reference 25 applying a first order homogenization scheme and displacement boundary conditions to the RVEs. Within the proposed framework the boundary value problems of the coarse and fine scale are coupled in such a way that the systems of nonlinear equations of both length scales can be solved optionally in a nested or simultaneous Newton iteration. The model is applied to sandwich plates with comb-like cores in Reference 26. For geometrical and material linear micro problems the homogenization procedure can be done for only one RVE in advance. This is also possible considering geometrical nonlinear shell macro problems.[27] A dependency of the transverse shear stiffness, shear stresses and associated resultants on the RVE length was observed for existing models in Reference 28. The undesired length dependencies follow from inevitable bending deformations which occur when transverse shear strains are applied to the RVE. To avoid this appropriate volumetric constraints have been developed.[29] As result a pure shear stress state is obtained in a first order two-scale model for beams. A second-order homogenization framework for thick shells adapting the orthogonality conditions[22] along with an additional constraint avoids likewise the length dependency of the transverse shear stiffness. Furthermore, a predictor-corrector scheme has to be applied for the transverse shear strains to obtain the correct values.[30]

A nonlinear multiscale model for Kirchhoff–Love shells is developed in Reference 31. An attached coordinate system for the projection of the strains enables the elimination of large rotations from the kinematic constraints that are imposed at the RVE. The contribution[32] picks up on an approach for a first order homogenization procedure based on the Irving-Kirkwood theory. Due to the possibility of using minimal boundary conditions whilst simultaneously reusing existing homogenization algorithms, creation of models and numerical implementation are straight forward. Within the so-called Direct FE2 the staggered two-scale simulations are condensed into a single finite element analysis, which facilitates the implementation in commercial FE codes.[33] The contribution deals with the modeling of thin–walled fiber reinforced composite laminates within the Mindlin–Reissner shell theory and Direct FE2. A multi-scale procedure for the mechanical analysis of flat laminates with discontinuities considering mixed boundary conditions is described in Reference 34. The publication[35] is concerned with a variationally consistent method to develop a homogenization framework for linear Reissner–Mindlin plates. The approach guarantees kinematically consistent prolongation and homogenization operations. In the recent contribution[36] three different types of boundary conditions, which fulfil the Hill–Mandel condition, are presented to bridge the two scales.

The essential features and new aspects of present formulation are summarized as follows:

(i) Based on our previous paper[25] we propose a first order homogenization scheme for Reissner–Mindlin shells that couples the boundary value problems at the coarse and fine scales in a variational setting. The associated weak form is consistently linearized whereby the resulting nonlinear FE equations of both scales can be solved in different ways.

As effective alternative to a nested iteration a simultaneous iteration procedure can be applied which also preserves quadratic convergence of Newton's method.

(ii) When applying periodic boundary conditions to RVEs in three-dimensional bodies rigid body movements are generally prevented by prescribed displacements of the corner nodes. This is not possible in present case as it causes localized distortions at the corners, and subsequently stress concentrations. The reason are the free surfaces. Thus, in present case stress boundary conditions are existent at the bottom and top surfaces of the RVEs, whereas at the lateral surfaces periodic boundary conditions are used. Appropriate constraint equations are developed which prevent both rigid body movements of the RVE and eliminate the above discussed length dependency of the transverse shear stiffness. Two versions with 5 or 9 constraint equations are described. The side conditions are fulfilled applying the Lagrange multiplier method.

(iii) The first of all linear formulation is extended to finite strain problems introducing some transformation relations for the stress resultants and the material matrix. The transformations are performed at each Gauss point on macro level.

(iv) For a homogeneous plate or shell and linear elasticity the material matrix for the stress resultants must be decoupled with respect to the submatrices for membrane, bending and shear. This important test is passed by means of a homogeneous RVE. The considered linear and nonlinear examples prove that the developed two–scale model is able to analyze the mechanical behavior of heterogeneous shell structures. We examine layered plates and shells and such with in-plane periodic structure.

2 | VARIATIONAL FORMULATION OF THE TWO–SCALE PROBLEM

Let $\mathcal{B}$ be the three–dimensional Euclidean space occupied by a shell with thickness h in the reference configuration. With ξ^i we denote a convected coordinate system of the body. The thickness coordinate $\xi^3 = z$ is defined in the range $h^- \leq z \leq h^+$, where h^- and h^+ are the thickness coordinates of the outer surfaces. Thus, an arbitrary reference surface Ω with boundary Γ is introduced. The coordinate on $\Gamma = \Gamma_\sigma \bigcup \Gamma_u$ is denoted by s. The shell is loaded statically by loads $\bar{\mathbf{p}}$ in Ω and by boundary forces $\bar{\mathbf{t}}$ on Γ_σ. The part of the boundary with prescribed displacements or rotations is denoted by Γ_u. In the following Latin and Greek indices range from 1 to 3 and 1 to 2, respectively. Commas denote partial differentiation with respect to ξ^i.

Position vectors of the initial reference surface and current surface are denoted by $\mathbf{X}_0(\xi^\alpha)$ and $\mathbf{x}_0(\xi^\alpha)$, respectively. Furthermore, a director field $\mathbf{N}(\xi^\alpha)$ with $|\mathbf{N}(\xi^\alpha)| = 1$ is introduced as a vector perpendicular to Ω. The director field $\mathbf{d}(\xi^\alpha)$ of the current configuration with $|\mathbf{d}(\xi^\alpha)| = 1$ is obtained by orthogonal transformations and is a function of the rotational parameters $\bar{\boldsymbol{\omega}}$. Within the Reissner–Mindlin theory transverse shear strains are accounted for, thus $\mathbf{x}_{0,\alpha} \cdot \mathbf{d} \neq 0$.

Hence, the displacement field follows from the difference of the position vectors in shell space

$$\bar{\mathbf{u}} = \bar{\mathbf{u}}_0 + z\,(\mathbf{d}(\bar{\boldsymbol{\omega}}) - \mathbf{N}) \qquad \bar{\mathbf{u}}_0 = \mathbf{x}_0 - \mathbf{X}_0. \tag{1}$$

The shell strains are derived in a standard way using kinematic assumption (1) and arranged in a vector as follows with $\bar{\mathbf{v}} = [\bar{\mathbf{u}}_0, \bar{\boldsymbol{\omega}}]^T$

$$\boldsymbol{\varepsilon}(\bar{\mathbf{v}}) = [\varepsilon_{11}, \varepsilon_{22}, 2\,\varepsilon_{12}, \kappa_{11}, \kappa_{22}, 2\,\kappa_{12}, \gamma_1, \gamma_2]^T. \tag{2}$$

The components are membrane strains $\varepsilon_{\alpha\beta}$, curvatures $\kappa_{\alpha\beta}$ and transverse shear strains γ_α

$$\begin{aligned} \varepsilon_{\alpha\beta} &= \frac{1}{2}(\mathbf{x}_{0,\alpha} \cdot \mathbf{x}_{0,\beta} - \mathbf{X}_{0,\alpha} \cdot \mathbf{X}_{0,\beta}), \\ \kappa_{\alpha\beta} &= \frac{1}{2}(\mathbf{x}_{0,\alpha} \cdot \mathbf{d}_{,\beta} + \mathbf{x}_{0,\beta} \cdot \mathbf{d}_{,\alpha} - \mathbf{X}_{0,\alpha} \cdot \mathbf{N}_{,\beta} - \mathbf{X}_{0,\beta} \cdot \mathbf{N}_{,\alpha}), \\ \gamma_\alpha &= \mathbf{x}_{0,\alpha} \cdot \mathbf{d} - \mathbf{X}_{0,\alpha} \cdot \mathbf{N}. \end{aligned} \tag{3}$$

The normal strains in thickness direction are zero due to the assumed inextensible director field.

A representative volume element (RVE) is introduced at an integration point i of a typical finite shell element according to Figure 1. The domain B_i extends through the total thickness h of the shell. In the following averaged quantities of the macro problem are indicated by an overbar. The displacement field is split in an averaged part $\bar{\mathbf{u}}$ and a fluctuation part $\tilde{\mathbf{u}}$

$$\mathbf{u} = \bar{\mathbf{u}} + \tilde{\mathbf{u}}. \tag{4}$$

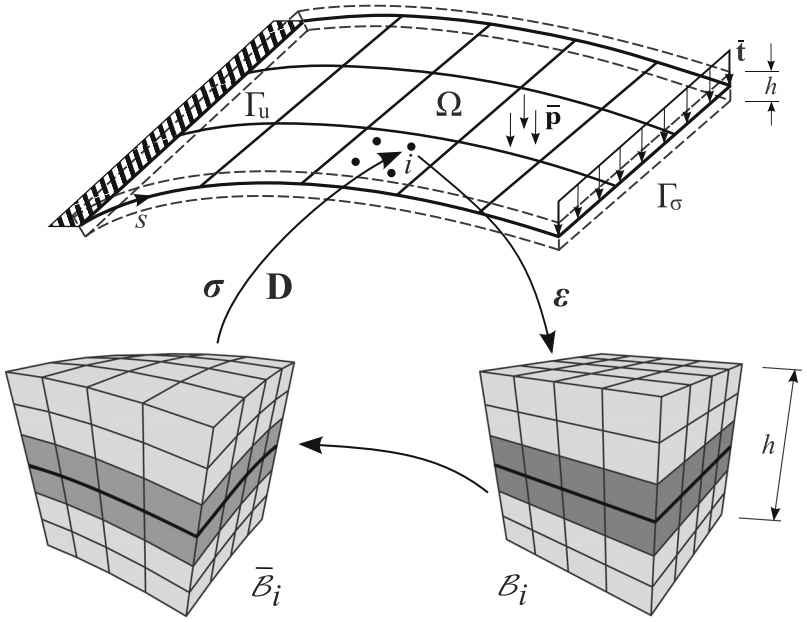

FIGURE 1 Computational homogenization of an inhomogeneous shell.

The averaged displacements $\bar{\mathbf{u}}$ according to (1) are linear in terms of the thickness coordinate, whereas the fluctuation part $\tilde{\mathbf{u}}$ describes warping and thickness change. Hence, the deformation gradient $\mathbf{F} = \mathbf{1} + \mathrm{Grad}\,\mathbf{u}$ is defined in a standard way and the Green–Lagrangian strain tensor $\mathbf{E}$ follows with $\mathbf{C} = \mathbf{F}^T\mathbf{F}$ as $\mathbf{E} = \frac{1}{2}(\mathbf{C} - \mathbf{1})$.

With the assumption of hyperelastic material behavior the following variational principle is introduced for the two-scale boundary value problem

$$\Pi(\bar{\mathbf{v}}, \mathbf{u}, \lambda) = \int_{(\Omega)} (\bar{W}(\boldsymbol{\varepsilon}) - \bar{\mathbf{p}} \cdot \bar{\mathbf{u}}_0)\,\mathrm{d}A - \int_{(\Gamma_\sigma)} \bar{\mathbf{t}} \cdot \bar{\mathbf{u}}_0\,\mathrm{d}s + \sum_{e=1}^{numel} \sum_{i=1}^{NGP} \frac{1}{A_0} \int_{(\Omega_i)} \int_{h^-}^{h^+} [W(\mathbf{C}) + \lambda \cdot \mathbf{g}]\,\mathrm{d}z\,\mathrm{d}A \to \mathrm{stat.}. \tag{5}$$

The first two terms refer to the macro problem (shell), whereas the third part is the contribution of the $numel \times NGP$ micro problems. Here, $numel$ denotes the total number of shell elements and NGP the number of Gauss points for each element. The area A_0 of the reference surface of the RVE follows with the in-plane measurements as $A_0 = l_x\, l_y$. On micro level existence of a strain energy density $W(\mathbf{C})$ is assumed. Averaging over the RVE leads to the macroscopic strain energy density $\bar{W}(\boldsymbol{\varepsilon})$. Constraint equations for the RVE are summarized in the vector $\mathbf{g}$ and are specified in the next section. In this context the vector of Lagrange multipliers λ is introduced. It is important to note that the constraints are fulfilled in an integral sense. The external loads $\bar{\mathbf{p}}$ and $\bar{\mathbf{t}}$ are assumed to be conservative.

Introducing $\boldsymbol{\theta} := [\bar{\mathbf{v}}, \mathbf{u}, \lambda]^T$ and admissible variations $\delta\boldsymbol{\theta} := [\delta\bar{\mathbf{v}}, \delta\mathbf{u}, \delta\lambda]^T$ the stationary condition associated with (5) reads

$$\begin{aligned}\delta\Pi(\boldsymbol{\theta}, \delta\boldsymbol{\theta}) := g(\boldsymbol{\theta}, \delta\boldsymbol{\theta}) = &\int_{(\Omega)} (\boldsymbol{\sigma} \cdot \delta\boldsymbol{\varepsilon} - \bar{\mathbf{p}} \cdot \delta\bar{\mathbf{u}}_0)\,\mathrm{d}A - \int_{(\Gamma_\sigma)} \bar{\mathbf{t}} \cdot \delta\bar{\mathbf{u}}_0\,\mathrm{d}s \\ &+ \sum_{e=1}^{numel} \sum_{i=1}^{NGP} \frac{1}{A_0} \int_{(\Omega_i)} \int_{h^-}^{h^+} [\mathbf{S} : \delta\mathbf{E} + \delta\lambda \cdot \mathbf{g} + \lambda \cdot \delta\mathbf{g}]\,\mathrm{d}z\,\mathrm{d}A = 0.\end{aligned} \tag{6}$$

The components of the vector $\boldsymbol{\sigma} = \partial_\epsilon \bar{W}$

$$\boldsymbol{\sigma} = \left[n^{11}, n^{22}, n^{12}, m^{11}, m^{22}, m^{12}, q^1, q^2\right]^T \tag{7}$$

are stress resultants with membrane forces $n^{\alpha\beta} = n^{\beta\alpha}$, bending moments $m^{\alpha\beta} = m^{\beta\alpha}$ and shear forces q^α. Variation of the shell strains (3) leads to

$$
\begin{aligned}
\delta\boldsymbol{\varepsilon} &= [\delta\varepsilon_{11}, \delta\varepsilon_{22}, 2\delta\varepsilon_{12}, \delta\kappa_{11}, \delta\kappa_{22}, 2\delta\kappa_{12}, \delta\gamma_1, \delta\gamma_2]^T \\
\delta\varepsilon_{\alpha\beta} &= \frac{1}{2}(\delta\mathbf{x}_{0,\alpha}\cdot\mathbf{x}_{0,\beta} + \delta\mathbf{x}_{0,\beta}\cdot\mathbf{x}_{0,\alpha}) \\
\delta\kappa_{\alpha\beta} &= \frac{1}{2}(\delta\mathbf{x}_{0,\alpha}\cdot\mathbf{d}_{,\beta} + \delta\mathbf{x}_{0,\beta}\cdot\mathbf{d}_{,\alpha} + \delta\mathbf{d}_{,\alpha}\cdot\mathbf{x}_{0,\beta} + \delta\mathbf{d}_{,\beta}\cdot\mathbf{x}_{0,\alpha}) \\
\delta\gamma_\alpha &= \delta\mathbf{x}_{0,\alpha}\cdot\mathbf{d} + \delta\mathbf{d}\cdot\mathbf{x}_{0,\alpha}\,.
\end{aligned}
\tag{8}
$$

Furthermore, $\mathbf{S} = 2\,\partial_{\mathbf{C}}W$ and $\delta\mathbf{E} = \frac{1}{2}(\delta\mathbf{F}^T\mathbf{F} + \mathbf{F}^T\delta\mathbf{F})$ denote the Second Piola–Kirchhoff stress tensor and the virtual Green–Lagrangian strain tensor, respectively. Integration by parts and application of standard arguments of variational calculus in Equation (6) yields the associated Euler–Lagrange equations. One obtains the static field equations and static boundary conditions in terms of stress resultants from the first two integrals. The last term in (6) yields the local equilibrium equations in terms of stresses as well as the static and geometric boundary conditions of the RVE.

For the finite element formulation of the next section we need to derive the linearization of stationary condition (6). One obtains

$$
\mathrm{L}\,[g(\boldsymbol{\theta}, \delta\boldsymbol{\theta}), \Delta\boldsymbol{\theta}] := g(\boldsymbol{\theta}, \delta\boldsymbol{\theta}) + \mathrm{D}g\cdot\Delta\boldsymbol{\theta},
\tag{9}
$$

where $g(\boldsymbol{\theta}, \delta\boldsymbol{\theta})$ is given in (6) and

$$
\begin{aligned}
\mathrm{D}g\cdot\Delta\boldsymbol{\theta} = &\int_{(\Omega)} (\Delta\boldsymbol{\sigma}\cdot\delta\boldsymbol{\varepsilon} + \boldsymbol{\sigma}\cdot\Delta\delta\boldsymbol{\varepsilon})\;\mathrm{d}A \\
&+ \sum_{e=1}^{numel}\sum_{i=1}^{NGP}\frac{1}{A_0}\int_{(\Omega_i)}\int_{h^-}^{h^+} (\Delta\mathbf{S}:\delta\mathbf{E} + \mathbf{S}:\Delta\delta\mathbf{E} + \delta\boldsymbol{\lambda}\cdot\Delta\mathbf{g} + \Delta\boldsymbol{\lambda}\cdot\delta\mathbf{g})\,\mathrm{d}z\,\mathrm{d}A
\end{aligned}
\tag{10}
$$

with $\Delta\boldsymbol{\sigma} = \mathbf{D}\;\Delta\boldsymbol{\varepsilon}$, $\Delta\mathbf{S} = \mathbb{C}\;\Delta\mathbf{E}$ and $\Delta\delta\mathbf{E} = \frac{1}{2}(\delta\mathbf{F}^T\Delta\mathbf{F} + \Delta\mathbf{F}^T\delta\mathbf{F})$. The matrix $\mathbb{C} = 2\,\partial_{\mathbf{C}}\mathbf{S}$ is a standard output of a library of constitutive laws in a material description. Concerning $\Delta\delta\boldsymbol{\varepsilon}$ we refer to the representation in Reference 37. The vector $\boldsymbol{\sigma}$ and the material matrix $\mathbf{D}$ as well as $\delta\mathbf{g}$ and $\Delta\mathbf{g}$ are specified consecutively.

3 | SMALL DEFORMATION ELASTIC PROBLEMS

In this section, we restrict ourselves to geometrical and material linear problems, The shell strains (3) are linearized and formulated with $\mathbf{w} = \mathbf{d} - \mathbf{N}$ as

$$
\begin{aligned}
\varepsilon_{\alpha\beta} &= \frac{1}{2}(\bar{\mathbf{u}}_{0,\alpha}\cdot\mathbf{X}_{0,\beta} + \bar{\mathbf{u}}_{0,\beta}\cdot\mathbf{X}_{0,\alpha}), \\
\kappa_{\alpha\beta} &= \frac{1}{2}(\bar{\mathbf{u}}_{0,\alpha}\cdot\mathbf{N}_{,\beta} + \bar{\mathbf{u}}_{0,\beta}\cdot\mathbf{N}_{,\alpha} + \mathbf{X}_{0,\alpha}\cdot\mathbf{w}_{,\beta} + \mathbf{X}_{0,\beta}\cdot\mathbf{w}_{,\alpha}), \\
\gamma_\alpha &= \bar{\mathbf{u}}_{0,\alpha}\cdot\mathbf{N} + \mathbf{X}_{0,\alpha}\cdot\mathbf{w}.
\end{aligned}
\tag{11}
$$

The components of $\mathbf{E}$ are the linear strains $E_{ij} = \frac{1}{2}(u_{i,j} + u_{j,i})$ and $\mathbf{S} = [\sigma_x, \sigma_y, \sigma_z, \sigma_{xy}, \sigma_{xz}, \sigma_{yz}]^T$ becomes the vector of linear stresses.

The strain energy density can be written as a quadratic form $W(\mathbf{E}) = \frac{1}{2}\;\mathbf{E}^T\;\mathbb{C}\;\mathbf{E}$. Assuming orthotropy the constitutive equations are given in the following standard manner using Voigt notation

$$
\begin{aligned}
&\partial_{\mathbf{E}}W = \mathbf{S} = \mathbb{C}\;\mathbf{E} \\
&\begin{bmatrix}\sigma_x\\ \sigma_y\\ \sigma_z\\ \sigma_{xy}\\ \sigma_{xz}\\ \sigma_{yz}\end{bmatrix} = \begin{bmatrix} C_{11} & C_{12} & C_{13} & C_{14} & 0 & 0\\ C_{21} & C_{22} & C_{23} & C_{24} & 0 & 0\\ C_{31} & C_{32} & C_{33} & C_{34} & 0 & 0\\ C_{41} & C_{42} & C_{43} & C_{44} & 0 & 0\\ 0 & 0 & 0 & 0 & C_{55} & C_{56}\\ 0 & 0 & 0 & 0 & C_{65} & C_{66}\end{bmatrix}\begin{bmatrix} u_{x,x}\\ u_{y,y}\\ u_{z,z}\\ u_{x,y}+u_{y,x}\\ u_{x,z}+u_{z,x}\\ u_{y,z}+u_{z,y}\end{bmatrix}.
\end{aligned}
\tag{12}
$$

The constants $C_{ij} = C_{ji}$ may depend on the thickness coordinate z. Transversely isotropic and isotropic material behavior are contained as special cases.

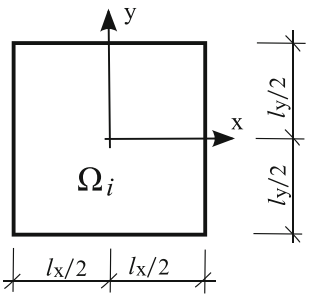

FIGURE 2 Reference surface of the RVE.

3.1 | Constraint equations for the micro problem

When applying transverse shear strains to the RVE one obtains besides shearing also bending deformations. This has been shown analytically by Klarmann et al.[29] by means of a beam model for the RVE. Besides a constant shear force also inevitably a linear moment distribution occurs. With increasing RVE length l_x or l_y, see Figure 2, the stored bending energy more and more dominates in comparison with the shear energy. In the consequence one obtains a decrease of the transverse shear stiffness. The dependency of the transverse shear stiffness on the RVE length is of course an inadmissible feature. To obtain a pure transverse shear strain state appropriate side conditions have to be developed.

To remedy the length dependency we introduce the following constraints adapting the approach for beams.[29] The key idea is explained here for the x-direction. The requirement

$$m_x := \int_{h^-}^{h^+} \sigma_x z \, \mathrm{d}z \stackrel{!}{=} \text{constant} \tag{13}$$

throughout the reference surface of the RVE is achieved with the constraint

$$\int_{-l_x/2}^{l_x/2} \int_{-l_y/2}^{l_y/2} m_x \, \kappa_x \, \mathrm{d}y \, \mathrm{d}x = 0. \tag{14}$$

When choosing a linear curvature $\kappa_x = \lambda \, x$ only a constant bending moment m_x can fulfill Equation (14) and hereby a linear shape of m_x is filtered out. The Lagrange parameter λ is constant in Ω_i and therefore can be taken out of the integral. The normal stress σ_x follows with elasticity law (12)

$$\sigma_x = C_{11} \, u_{x,x} + C_{12} \, u_{y,y} + C_{13} \, u_{z,z} + C_{14} \, (u_{x,y} + u_{y,x}). \tag{15}$$

It is inserted into (13) and the result in (14). The term $x \, C_{11} \, u_{x,x} \, z$ is integrated by parts with respect to x

$$\begin{aligned} \int_{-l_x/2}^{l_x/2} \int_{-l_y/2}^{l_y/2} \int_{h^-}^{h^+} x \, C_{11}(z) \, u_{x,x} \, z \, \mathrm{d}z \, \mathrm{d}y \, \mathrm{d}x = &- \int_{-l_x/2}^{l_x/2} \int_{-l_y/2}^{l_y/2} \int_{h^-}^{h^+} C_{11}(z) \, u_x \, z \, \mathrm{d}z \, \mathrm{d}y \, \mathrm{d}x \\ &+ \int_{-l_y/2}^{l_y/2} \int_{h^-}^{h^+} [x \, C_{11}(z) \, u_x(x,y,z) \, z]_{x=-l_x/2}^{x=l_x/2} \, \mathrm{d}z \, \mathrm{d}y = 0 \\ g = g_1 + g_2 = 0. & \end{aligned} \tag{16}$$

Only the surfaces at $x = \pm l_x/2$ enter into the surface integral g_2, since at the other surfaces of the RVE the component n_x of the unit normal vector is zero. The term $x \, z \, [C_{12} \, u_{y,y} + C_{13} \, u_{z,z} + C_{14}(u_{x,y} + u_{y,x})]$ remains unchanged.

Remark. With the right hand side of (16) as part of the constraint equations rigid body rotations about the y-axis are automatically suppressed. This follows from the fact that with $C_{11} > 0$ the volume integral g_1 can only vanish if a rigid body rotation $u_x = \alpha_y\, z$ does not occur. Here, α_y is an infinitesimal angle about the y-axis. Hence the surface integral g_2 is also zero for the aforementioned rigid body rotation as the same integrand appears with $x = \pm l_x/2 =$ constant. Thus, both conditions $m_x =$ constant and $\alpha_y = 0$ are fulfilled with $g_1 = 0$. The introduction of further constraints to prevent the rigid body rotation is not necessary. Within present approach both the length dependency of the transverse shear stiffness and rigid body movements are eliminated.

In an analogues way the constraint $m_y =$ constant is handled. When coupling between bending and membrane deformation occurs additionally $n_x =$ constant and $n_y =$ constant have to be considered. Furthermore, besides the four conditions

$$\begin{aligned} m_x &= \int_{h^-}^{h^+} \sigma_x z \, \mathrm{d}z \stackrel{!}{=} \text{constant}, \\ m_y &= \int_{h^-}^{h^+} \sigma_y z \, \mathrm{d}z \stackrel{!}{=} \text{constant}, \\ n_x &= \int_{h^-}^{h^+} \sigma_x \, \mathrm{d}z \stackrel{!}{=} \text{constant}, \\ n_y &= \int_{h^-}^{h^+} \sigma_y \, \mathrm{d}z \stackrel{!}{=} \text{constant}, \end{aligned} \tag{17}$$

rigid body movements in z-direction have to be suppressed. This is achieved when the integral of u_z vanishes. Due to the three-dimensional material law likewise four further integrals of $u_{z,z}$ weighted with x, y, z have to be considered.

Now we can summarize the 9 components of the vector $\mathbf{g}$ as is introduced in (5)

$$\mathbf{g} = \begin{bmatrix} \{-C_{11}\, u_x + x\, (C_{12}\, u_{y,y} + C_{13}\, u_{z,z} + C_{14}\, (u_{x,y} + u_{y,x})\}\, z \\ \{-C_{22}\, u_y + y\, (C_{21}\, u_{x,x} + C_{23}\, u_{z,z} + C_{24}\, (u_{x,y} + u_{y,x})\}\, z \\ -C_{11}\, u_x + x\, (C_{12}\, u_{y,y} + C_{13}\, u_{z,z} + C_{14}\, (u_{x,y} + u_{y,x}) \\ -C_{22}\, u_y + y\, (C_{21}\, u_{x,x} + C_{23}\, u_{z,z} + C_{24}\, (u_{x,y} + u_{y,x}) \\ u_z \\ x\, z\, u_{z,z} \\ y\, z\, u_{z,z} \\ x\, u_{z,z} \\ y\, u_{z,z} \end{bmatrix}. \tag{18}$$

The Lagrange parameters associated with the 3rd, 4th, 8th, and 9th component of $\mathbf{g}$ are only unequal zero if coupling between membrane and bending deformation occurs. This is for example, the case for an eccentric reference surface or a nonsymmetric stacking sequence of a laminate. The 1st and 2nd component eliminate rigid body rotations about the y- and x-axis as well as the 3rd, 4th, and 5th component rigid body translations in x, y and z-direction, respectively. The rigid body rotation about the z-axis is suppressed by in-plane link conditions. These are specified below when discussing periodic boundary conditions.

It is possible to omit the last four components containing $u_{z,z}$, thus only the first 5 components in (18) remain. This can be done by elimination of $u_{z,z}$ via $\sigma_z = C_{31}\, u_{x,x} + C_{32}\, u_{y,y} + C_{33}\, u_{z,z} + C_{34}\, (u_{x,y} + u_{y,x}) = 0$. When replacing C_{ij} by the constants

$$\overline{C}_{ij} = \overline{C}_{ji} = C_{ij} - C_{i3} C_{3j} / C_{33}, \qquad \overline{C}_{i3} = \overline{C}_{3i} = 0 \tag{19}$$

of the 2D material law one obtains also correct results for the homogenized material matrices, see the examples in Section 6.

3.2 | FE approximations of the constraint equations

The finite element ansatz for the displacements $\mathbf{u} = [u_x, u_y, u_z]^T$ of the micro problem reads

$$\mathbf{u}^h = \sum_{I=1}^{nel} N_I \, \mathbf{v}_I \qquad \mathbf{v}_I = [u_{xI}, u_{yI}, u_{zI}]^T, \tag{20}$$

where $nel \in \{8, 27, 64\}$ denotes the number of nodes per element. The superscript h refers to the finite element approximation. The shape functions N_I are tri-linear, tri-quadratic or tri-cubic functions of the normalized coordinates $-1 \leq \{\xi, \eta, \zeta\} \leq 1$, respectively.

Inserting the ansatz $\mathbf{u}^h$ into (18) yields

$$\mathbf{g} = \mathbf{h} \, \mathbf{v}_e = \sum_{I=1}^{nel} \mathbf{h}_I \, \mathbf{v}_I \tag{21}$$

with $\mathbf{h} = [\mathbf{h}_1, \ldots, \mathbf{h}_I, \ldots, \mathbf{h}_{nel}]$, $\mathbf{v}_e = [\mathbf{v}_1, \ldots, \mathbf{v}_I, \ldots, \mathbf{v}_{nel}]^T$ and

$$\mathbf{h}_I = \begin{bmatrix} \{-C_{11} \, N_I \, \mathbf{e}_x^T + x \, (C_{12} \, N_{I,y} \, \mathbf{e}_y^T + C_{13} \, N_{I,z} \, \mathbf{e}_z^T + C_{14} \, (N_{I,y} \, \mathbf{e}_x^T + N_{I,x} \, \mathbf{e}_y^T)\} \, z \\ \{-C_{22} \, N_I \, \mathbf{e}_y^T + y \, (C_{21} \, N_{I,x} \, \mathbf{e}_x^T + C_{23} \, N_{I,z} \, \mathbf{e}_z^T + C_{24} \, (N_{I,y} \, \mathbf{e}_x^T + N_{I,x} \, \mathbf{e}_y^T)\} \, z \\ -C_{11} \, N_I \, \mathbf{e}_x^T + x \, (C_{12} \, N_{I,y} \, \mathbf{e}_y^T + C_{13} \, N_{I,z} \, \mathbf{e}_z^T + C_{14} \, (N_{I,y} \, \mathbf{e}_x^T + N_{I,x} \, \mathbf{e}_y^T) \\ -C_{22} \, N_I \, \mathbf{e}_y^T + y \, (C_{21} \, N_{I,x} \, \mathbf{e}_x^T + C_{23} \, N_{I,z} \, \mathbf{e}_z^T + C_{24} \, (N_{I,y} \, \mathbf{e}_x^T + N_{I,x} \, \mathbf{e}_y^T) \\ N_I \, \mathbf{e}_z^T \\ x \, z \, N_{I,z} \, \mathbf{e}_z^T \\ y \, z \, N_{I,z} \, \mathbf{e}_z^T \\ x \, N_{I,z} \, \mathbf{e}_z^T \\ y \, N_{I,z} \, \mathbf{e}_z^T \end{bmatrix} \tag{22}$$

as well as the Cartesian base vectors $\{\mathbf{e}_x, \mathbf{e}_y, \mathbf{e}_z\}$. When omitting the last four components in $\mathbf{h}_I$ the elasticity constants C_{ij} are replaced by $\bar{C}_{ij}$ according to Equation (19). As $\mathbf{h}$ does not depend on the displacements it holds

$$\delta\mathbf{g} = \mathbf{h} \, \delta\mathbf{v}_e, \qquad \Delta\mathbf{g} = \mathbf{h} \, \Delta\mathbf{v}_e. \tag{23}$$

In the following we consider the Lagrange terms in the linearized weak form (9) along with (6) and (10). The vector λ is constant throughout the RVE. Inserting Equations (21) and (23) into the Lagrange terms yields

$$\begin{aligned} &\int_{(V_e)} [\delta\lambda \cdot (\mathbf{g} + \Delta\mathbf{g}) + \delta\mathbf{g} \cdot (\lambda + \Delta\lambda)] \, \mathrm{d}V \\ &= \int_{(V_e)} \left\{ \begin{bmatrix} \delta\mathbf{v}_e \\ \delta\lambda \end{bmatrix}^T \begin{bmatrix} \mathbf{0} & \mathbf{h}^T \\ \mathbf{h} & \mathbf{0} \end{bmatrix} \begin{bmatrix} \Delta\mathbf{v}_e \\ \Delta\lambda \end{bmatrix} + \begin{bmatrix} \mathbf{h}^T \, \lambda \\ \mathbf{h} \, \mathbf{v}_e \end{bmatrix} \right\} \mathrm{d}V \\ &= \delta\hat{\mathbf{v}}_e^T (\hat{\mathbf{k}}_e^c \, \Delta\hat{\mathbf{v}}_e + \hat{\mathbf{f}}_e^c), \end{aligned} \tag{24}$$

where V_e denotes the domain of one element and $\mathrm{d}V = \mathrm{d}z \, \mathrm{d}A$. The displacements and Lagrange multipliers are summarized within the generalized displacement vector $\hat{\mathbf{v}}_e = [\mathbf{v}_e, \lambda]^T$. In an analogues way $\delta\hat{\mathbf{v}}_e = [\delta\mathbf{v}_e, \delta\lambda]^T$ and $\Delta\hat{\mathbf{v}}_e = [\Delta\mathbf{v}_e, \Delta\lambda]^T$ are introduced. In the following the matrices and vectors related to the generalized vectors are denoted by the hat symbol. The element matrix $\hat{\mathbf{k}}_e^c$ and the element vector $\hat{\mathbf{f}}_e^c$

$$\hat{\mathbf{k}}_e^c = \int_{(V_e)} \begin{bmatrix} \mathbf{0} & \mathbf{h}^T \\ \mathbf{h} & \mathbf{0} \end{bmatrix} \mathrm{d}V, \qquad \hat{\mathbf{f}}_e^c = \int_{(V_e)} \begin{bmatrix} \mathbf{h}^T \lambda \\ \mathbf{h} \, \mathbf{v}_e \end{bmatrix} \mathrm{d}V \tag{25}$$

consider the constraint part of the variational formulation and can be programmed as a separate finite element code. Hence, they are assembled with solid elements or solid shell elements to the global stiffness matrix and the global residual vector of the RVE. The alternative is to add the programming of $\hat{\mathbf{k}}_e^c$ and $\hat{\mathbf{f}}_e^c$ in existing solid elements or solid shell elements. The 9 Lagrange parameters are associated with three global nodes which are shared by all elements of the RVE, see

Reference 29. When only 5 parameters are used two nodes are sufficient, and the main diagonal stiffness associated with the not used degree of freedom is set to one to avoid singular matrices. As an example, when using 9 constraints and tri-quadratic ansatz functions for the displacements, $\hat{\mathbf{k}}_e^c$ is the stiffness matrix of a n–noded finite element with $n = 27 + 3 = 30$ and thereby the size of $\hat{\mathbf{k}}_e^c$ is $3\,n \times 3\,n$.

3.3 | Boundary conditions on the RVE

In the following the boundary conditions for the RVE are specified. The Hill condition[38] requires the equivalence of the microscopic and macroscopic stress power. With application of the Gauss theorem an alternative representation in terms of a surface integral can be derived. This shows that stress boundary conditions, displacement boundary conditions and periodic boundary conditions are conform with the Hill condition, for example, References 1 and 2. Especially for sandwich shells with a weak core displacement boundary conditions lead to an unacceptable stiff behavior. Stress boundary conditions on the surfaces can be applied in a strain driven algorithm using the macroscopic stresses or stress resultants as Lagrange multipliers, respectively. This requires the consideration of a surface integral on the RVE. Rigid body motions can be excluded adding some artificial constraints.[9]

In this paper only periodic boundary conditions are considered. The coordinates of the RVE are bounded by

$$-l_x/2 \le x \le l_x/2, \qquad -l_y/2 \le y \le l_y/2, \qquad h^- \le z \le h^+. \tag{26}$$

The lower surface $z = h^-$ and the upper surface $z = h^+$ are free of stresses. This is approximately fulfilled within the finite element solution and is improved by mesh refinement in a standard way. For some special cases the stress boundary conditions at $z = h^-, z = h^+$ are fulfilled in an exact way.

The periodic boundary conditions at the lateral surfaces read with $\mathbf{X} := [x, y, z]^T$

$$\left.\begin{aligned} \mathbf{u} &= \bar{\mathbf{E}}\,\mathbf{X} + \tilde{\mathbf{u}} \\ \tilde{\mathbf{u}}^+ &= \tilde{\mathbf{u}}^- \end{aligned}\right\} \quad \text{at} \quad \begin{aligned} x &= \pm l_x/2, \\ y &= \pm l_y/2, \end{aligned} \tag{27}$$

The superscripts + and − refer to the surfaces $x = l_x/2, y = l_y/2$ and $x = -l_x/2, y = -l_y/2$, respectively. Recall that in this section small deformation problems with linear strain measures $\bar{\mathbf{E}}$ are considered. Equation $(27)_1$ is evaluated at $\mathbf{X} = \mathbf{X}^+$ and $\mathbf{X} = \mathbf{X}^-$. This leads with $\tilde{\mathbf{u}}^+ = \tilde{\mathbf{u}}^-$ and $\Delta\mathbf{X} = \mathbf{X}^+ - \mathbf{X}^-$ to

$$\begin{aligned} \mathbf{u}^+ &= \mathbf{u}^- + \bar{\mathbf{E}}\,\Delta\mathbf{X}, \\ \begin{bmatrix} u_x^+ \\ u_y^+ \\ u_z^+ \end{bmatrix} &= \begin{bmatrix} u_x^- \\ u_y^- \\ u_z^- \end{bmatrix} + \begin{bmatrix} \bar{E}_{11} & \bar{E}_{12} & \bar{E}_{13} \\ \bar{E}_{21} & \bar{E}_{22} & \bar{E}_{23} \\ \bar{E}_{31} & \bar{E}_{32} & \bar{E}_{33} \end{bmatrix} \begin{bmatrix} \Delta x \\ \Delta y \\ \Delta z \end{bmatrix}. \end{aligned} \tag{28}$$

Inserting the relations of $\bar{E}_{ij}$ to the shell strains

$$\begin{aligned} \bar{E}_{11} &= \varepsilon_{11} + z\,\kappa_{11}, \\ \bar{E}_{22} &= \varepsilon_{22} + z\,\kappa_{22}, \\ \bar{E}_{33} &= 0, \\ \bar{E}_{12} &= \bar{E}_{21} = \varepsilon_{12} + z\,\kappa_{12}, \\ 2\,\bar{E}_{13} &= 2\,\bar{E}_{31} = 2\,\varepsilon_{13} = \gamma_1, \\ 2\,\bar{E}_{23} &= 2\,\bar{E}_{32} = 2\,\varepsilon_{23} = \gamma_2, \end{aligned} \tag{29}$$

into (28) yields

$$\begin{bmatrix} u_x^+ \\ u_y^+ \\ u_z^+ \end{bmatrix} = \begin{bmatrix} u_x^- \\ u_y^- \\ u_z^- \end{bmatrix} + \begin{bmatrix} \varepsilon_{11} + z\,\kappa_{11} & \varepsilon_{12} + z\,\kappa_{12} & \varepsilon_{13} \\ \varepsilon_{12} + z\,\kappa_{12} & \varepsilon_{22} + z\,\kappa_{22} & \varepsilon_{23} \\ \varepsilon_{13} & \varepsilon_{23} & 0 \end{bmatrix} \begin{bmatrix} \Delta x \\ \Delta y \\ \Delta z \end{bmatrix}. \tag{30}$$

It holds $z^+ = z^-$ for the nodes on opposite surfaces $x = \pm l_x/2$ and $y = \pm l_y/2$, thus $\Delta z = 0$. Therefore Equation (30) has to be modified as follows, see also the approach for beams[29]:

$$\begin{bmatrix} u_x^+ \\ u_y^+ \\ u_z^+ \end{bmatrix} = \begin{bmatrix} u_x^- \\ u_y^- \\ u_z^- \end{bmatrix} + \begin{bmatrix} \varepsilon_{11} + z\,\kappa_{11} & \varepsilon_{12} + z\,\kappa_{12} & 0 \\ \varepsilon_{12} + z\,\kappa_{12} & \varepsilon_{22} + z\,\kappa_{22} & 0 \\ 2\,\varepsilon_{13} & 2\,\varepsilon_{23} & 0 \end{bmatrix} \begin{bmatrix} \Delta x \\ \Delta y \\ \Delta z \end{bmatrix}. \tag{31}$$

Equation (31) is rewritten using the vector of shell strains (2) with the components (11)

$$\begin{bmatrix} u_x^+ \\ u_y^+ \\ u_z^+ \end{bmatrix} = \begin{bmatrix} u_x^- \\ u_y^- \\ u_z^- \end{bmatrix} + \begin{bmatrix} \Delta x & 0 & \frac{1}{2}\Delta y & \Delta x\, z & 0 & \frac{1}{2}\Delta y\, z & 0 & 0 \\ 0 & \Delta y & \frac{1}{2}\Delta x & 0 & \Delta y\, z & \frac{1}{2}\Delta x\, z & 0 & 0 \\ 0 & 0 & 0 & 0 & 0 & 0 & \Delta x & \Delta y \end{bmatrix} \begin{bmatrix} \varepsilon_{11} \\ \varepsilon_{22} \\ 2\varepsilon_{12} \\ \kappa_{11} \\ \kappa_{22} \\ 2\kappa_{12} \\ \gamma_1 \\ \gamma_2 \end{bmatrix}, \tag{32}$$

$$\mathbf{u}^+ = \mathbf{u}^- + \mathbf{A}(\Delta x, \Delta y, z)\ \boldsymbol{\varepsilon}.$$

To realize $\tilde{\mathbf{u}}^+ = \tilde{\mathbf{u}}^-$ according to $(27)_2$ link conditions have to be applied to the RVE. The in-plane displacements are linked in a standard symmetric manner. In contrast to that out of plane displacements of nodes with same coordinates z on two opposite surfaces have to be linked with respect to the coordinates x and y in an antisymmetric way, see Table 1. It has been shown in the framework of a first order homogenization approach[25] that symmetric link conditions for $\tilde{u}_z$ lead to restraints of the torsion deformation and consequential to wrong results for the torsion stiffness.

Remark. The link conditions $\tilde{\mathbf{u}}^+ = \tilde{\mathbf{u}}^-$ are fulfilled applying the well-known master slave approach. Thus, $\tilde{\mathbf{u}}^+$ is eliminated and only $\tilde{\mathbf{u}}^-$ enters into the FE equations. In Equation (32) the displacements $\mathbf{u}^+$ of a slave node are back substituted from the displacements $\mathbf{u}^-$ of a master node and the product term $\mathbf{A}\,\boldsymbol{\varepsilon}$. Note that Δx and Δy are different for symmetric and antisymmetric link conditions. As a consequence Δx and Δy from the first and second row of $\mathbf{A}$ distinguish from those values of the third row.

Finally we introduce the element matrix $\mathbf{A}_e$ with submatrices $\boldsymbol{\delta}_I$ and $\mathbf{A}_I$ where $1 \le I \le nel$ as well as $nel \in \{8, 27, 64\}$:

$$\mathbf{A}_e = \begin{bmatrix} \boldsymbol{\delta}_1\ \mathbf{A}_1 \\ \vdots \\ \boldsymbol{\delta}_I\ \mathbf{A}_I \\ \vdots \\ \boldsymbol{\delta}_{nel}\ \mathbf{A}_{nel} \end{bmatrix}_{(3\ nel \times 8)} \quad \boldsymbol{\delta}_I = \begin{bmatrix} \delta_{1I} & 0 & 0 \\ 0 & \delta_{2I} & 0 \\ 0 & 0 & \delta_{3I} \end{bmatrix} \quad \mathbf{A}_I = \begin{bmatrix} \Delta x^s & 0 & \frac{1}{2}\Delta y^s & \Delta x^s z & 0 & \frac{1}{2}\Delta y^s z & 0 & 0 \\ 0 & \Delta y^s & \frac{1}{2}\Delta x^s & 0 & \Delta y^s z & \frac{1}{2}\Delta x^s z & 0 & 0 \\ 0 & 0 & 0 & 0 & 0 & 0 & \Delta x^a & \Delta y^a \end{bmatrix}. \tag{33}$$

$$\delta_{jI} = \begin{cases} 1\,, & \text{if DOF } j \text{ of node } I \text{ is linked to a master node} \\ 0\,, & \text{else} \end{cases}$$

The superscripts s and a refer to symmetric and antisymmetric link conditions, respectively. For all inner elements of the RVE follows $\mathbf{A}_e = \mathbf{0}$.

TABLE 1 Link conditions for an RVE.

Nodes I on	Link condition
Faces: $x = -l_x/2,\ x = l_x/2$	$\tilde{u}_\alpha(l_x/2, y, z) = \tilde{u}_\alpha(-l_x/2, y, z)\alpha = x, y$
	$\tilde{u}_z(l_x/2, y, z) = \tilde{u}_z(-l_x/2, -y, z)$
Faces: $y = -l_y/2,\ y = l_y/2$	$\tilde{u}_\alpha(x, l_y/2, z) = \tilde{u}_\alpha(x, -l_y/2, z)$
	$\tilde{u}_z(x, l_y/2, z) = \tilde{u}_z(-x, -l_y/2, z)$

4 | FINITE ELEMENT FORMULATION OF THE TWO-SCALE PROBLEM

We describe a finite element formulation based on a standard displacement method. In the examples of Section 6 also mixed elements are used. Concerning mixed hybrid element formulations for layered shells we refer to Reference 39.

The reference surface of the shell is discretized with *numel* quadrilateral shell elements

$$\Omega^h = \sum_{e=1}^{numel} \Omega_e. \tag{34}$$

Initial geometry, displacements and rotations are interpolated with bilinear functions which are arranged in the shape function matrix $\mathbf{N}$. The nodal degrees of freedom are three displacements and two or three rotations. At nodes on shell intersections, kinks or folds three global rotations are present, whereas at the other nodes two local rotations are used. With incorporation of the assumed shear strain interpolation[40] shear locking can be avoided in case of thin shells.

In this section we use the superscripts M and m for the macro and micro problems, respectively. Inserting the ansatz functions for the displacements and virtual displacements into the linearized weak form (9) considering (6) and (10) yields

$$\mathrm{L}\left[g(\boldsymbol{\theta}^h, \delta\boldsymbol{\theta}^h), \Delta\boldsymbol{\theta}^h\right] = \sum_{e=1}^{numel} \begin{bmatrix} \delta\mathbf{v}^M \\ \delta\bar{\mathbf{V}}_1^m \\ \vdots \\ \delta\bar{\mathbf{V}}_i^m \\ \vdots \\ \delta\bar{\mathbf{V}}_{NGP}^m \end{bmatrix}_e^T \left\{ \begin{bmatrix} \mathbf{k}^M & \mathbf{0} & \vdots & \mathbf{0} & \vdots & \mathbf{0} \\ \mathbf{0} & \mathbf{K}_1^m & \vdots & \mathbf{0} & \vdots & \mathbf{0} \\ \cdots & \cdots & \ddots & \mathbf{0} & \cdots & \cdots \\ \mathbf{0} & \mathbf{0} & \mathbf{0} & \mathbf{K}_i^m & \mathbf{0} & \mathbf{0} \\ \cdots & \cdots & \cdots & \mathbf{0} & \ddots & \cdots \\ \mathbf{0} & \mathbf{0} & \cdots & \mathbf{0} & \cdots & \mathbf{K}_{NGP}^m \end{bmatrix}_e \begin{bmatrix} \Delta\mathbf{v}^M \\ \Delta\bar{\mathbf{V}}_1^m \\ \vdots \\ \Delta\bar{\mathbf{V}}_i^m \\ \vdots \\ \Delta\bar{\mathbf{V}}_{NGP}^m \end{bmatrix}_e + \begin{bmatrix} \mathbf{f}^M \\ \mathbf{F}_1^m \\ \vdots \\ \mathbf{F}_i^m \\ \vdots \\ \mathbf{F}_{NGP}^m \end{bmatrix}_e \right\}_e . \tag{35}$$

The part with superscript M follows from the macro problem of the linearized weak form (9). The element residual vector and the tangential element stiffness matrix read

$$\mathbf{f}^M(\boldsymbol{\sigma}_i) = \int_{(\Omega_e)} (\mathbf{B}^T\boldsymbol{\sigma} - \mathbf{N}^T\bar{\mathbf{p}})\,\mathrm{d}A - \int_{(\Gamma_{\sigma e})} \mathbf{N}^T\bar{\mathbf{t}}\,\mathrm{d}s \qquad \mathbf{k}^M(\mathbf{D}_i) = \int_{(\Omega_e)} (\mathbf{B}^T\mathbf{D}\,\mathbf{B} + \mathbf{G})\,\mathrm{d}A. \tag{36}$$

Concerning the matrices $\mathbf{B}$ and $\mathbf{G}$ we refer to Reference 37. The vector of stress resultants $\boldsymbol{\sigma}_i$ and the material matrix $\mathbf{D}_i$ are specified below.

The contributions of the second to the last row in (35) are associated with the micro problems at Gauss points $1 \le i \le NGP$ of shell element e. We continue with the contribution of Gauss point i

$$\delta\bar{\mathbf{V}}_i^{mT}\ \left(\mathbf{K}_i^m\ \Delta\bar{\mathbf{V}}_i^m + \mathbf{F}_i^m\right) = \frac{1}{A_0}\sum_{e=1}^{N} \delta\hat{\mathbf{v}}_e^T \left(\hat{\mathbf{k}}_e^m\ \Delta\hat{\mathbf{v}}_e + \hat{\mathbf{f}}_e^m\right). \tag{37}$$

Here, the total number of elements used for the discretization of the RVE is denoted by N. The tangential element stiffness matrix $\hat{\mathbf{k}}_e^m = \hat{\mathbf{k}}_e + \hat{\mathbf{k}}_e^c$ and the element residual vector $\hat{\mathbf{f}}_e^m = \hat{\mathbf{f}}_e + \hat{\mathbf{f}}_e^c$ contain the contributions of the constraints $\hat{\mathbf{k}}_e^c$ and $\hat{\mathbf{f}}_e^c$ according to Equation (25). The element matrices $\hat{\mathbf{k}}_e$ and $\hat{\mathbf{f}}_e$ of standard solid elements with 27 or 64 nodes as well as of 8-noded solid shell elements are only populated in the range of the displacement degrees of freedom.

The relation of the generalized element displacement vector $\hat{\mathbf{v}}_e$ to the macroscopic shell strains $\boldsymbol{\varepsilon}_i$ and the generalized displacement vector $\hat{\mathbf{V}}_i^m$ follows with (27)

$$\hat{\mathbf{v}}_e = \hat{\mathbf{A}}_e\ \boldsymbol{\varepsilon}_i + \hat{\mathbf{a}}_e\ \hat{\mathbf{V}}_i^m, \qquad \hat{\mathbf{A}}_e = \begin{bmatrix} \mathbf{A}_e \\ \mathbf{0} \end{bmatrix}, \qquad \hat{\mathbf{V}}_i^m = \begin{bmatrix} \mathbf{V}_i^m \\ \lambda \end{bmatrix}. \tag{38}$$

Here $\hat{\mathbf{a}}_e$ denotes a standard assembly matrix and $\mathbf{A}_e$ is specified in (33). The associated variation and linearization

$$\delta\hat{\mathbf{v}}_e = \left[\hat{\mathbf{a}}_e, \hat{\mathbf{A}}_e\right] \begin{bmatrix} \delta\hat{\mathbf{V}}_i^m \\ \delta\boldsymbol{\varepsilon}_i \end{bmatrix}, \qquad \Delta\hat{\mathbf{v}}_e = \left[\hat{\mathbf{a}}_e, \hat{\mathbf{A}}_e\right] \begin{bmatrix} \Delta\hat{\mathbf{V}}_i^m \\ \Delta\boldsymbol{\varepsilon}_i \end{bmatrix} \tag{39}$$

are inserted into (37)

$$\begin{aligned}
&\delta\bar{\mathbf{V}}_i^{mT}\ \left(\mathbf{K}_i^m\ \Delta\bar{\mathbf{V}}_i^m + \mathbf{F}_i^m\right)\\
&= \frac{1}{A_0}\sum_{e=1}^{N}\begin{bmatrix}\delta\hat{\mathbf{V}}_i^m\\ \delta\boldsymbol{\varepsilon}_i\end{bmatrix}^T\left\{\begin{bmatrix}\hat{\mathbf{a}}_e^T\,\hat{\mathbf{k}}_e^m\,\hat{\mathbf{a}}_e & \hat{\mathbf{a}}_e^T\,\hat{\mathbf{k}}_e^m\,\hat{\mathbf{A}}_e\\ \hat{\mathbf{A}}_e^T\,\hat{\mathbf{k}}_e^m\,\hat{\mathbf{a}}_e & \hat{\mathbf{A}}_e^T\,\hat{\mathbf{k}}_e^m\,\hat{\mathbf{A}}_e\end{bmatrix}_e\begin{bmatrix}\Delta\hat{\mathbf{V}}_i\\ \Delta\boldsymbol{\varepsilon}_i\end{bmatrix} + \begin{bmatrix}\hat{\mathbf{a}}_e^T\,\hat{\mathbf{f}}_e^m\\ \hat{\mathbf{A}}_e^T\,\hat{\mathbf{f}}_e^m\end{bmatrix}_e\right\}\\
&= \frac{1}{A_0}\begin{bmatrix}\delta\hat{\mathbf{V}}_i^m\\ \delta\boldsymbol{\varepsilon}_i\end{bmatrix}^T\left\{\begin{bmatrix}\mathbf{K}_{11} & \mathbf{K}_{12}\\ \mathbf{K}_{21} & \mathbf{K}_{22}\end{bmatrix}\begin{bmatrix}\Delta\hat{\mathbf{V}}_i^m\\ \Delta\boldsymbol{\varepsilon}_i\end{bmatrix} + \begin{bmatrix}\mathbf{F}_1\\ \mathbf{F}_2\end{bmatrix}\right\}.
\end{aligned} \tag{40}$$

To alleviate the notation the Gauss point index i is omitted in the following matrices

$$\begin{aligned}
\mathbf{K}_{11} &= \sum_{e=1}^{N}\hat{\mathbf{a}}_e^T\,\hat{\mathbf{k}}_e^m\,\hat{\mathbf{a}}_e, & \mathbf{K}_{21} &= \mathbf{K}_{12}^T,\\
\mathbf{K}_{12} &= \sum_{e=1}^{N}\hat{\mathbf{a}}_e^T\,\hat{\mathbf{k}}_e^m\,\hat{\mathbf{A}}_e, & \mathbf{F}_1 &= \sum_{e=1}^{N}\hat{\mathbf{a}}_e^T\,\hat{\mathbf{f}}_e^m,\\
\mathbf{K}_{22} &= \sum_{e=1}^{N}\hat{\mathbf{A}}_e^T\,\hat{\mathbf{k}}_e^m\,\hat{\mathbf{A}}_e, & \mathbf{F}_2 &= \sum_{e=1}^{N}\hat{\mathbf{A}}_e^T\,\hat{\mathbf{f}}_e^m.
\end{aligned} \tag{41}$$

With $\delta\hat{\mathbf{V}}_i^m \neq \mathbf{0}$ the incremental generalized displacement vector $\Delta\hat{\mathbf{V}}_i^m$ can be eliminated from the set of equations via $\mathbf{K}_{11}\ \Delta\hat{\mathbf{V}}_i^m + \mathbf{K}_{12}\ \Delta\boldsymbol{\varepsilon}_i + \mathbf{F}_1 = \mathbf{0}$ which yields

$$\Delta\hat{\mathbf{V}}_i^m = -\mathbf{K}_{11}^{-1}\ (\mathbf{F}_1 + \mathbf{K}_{12}\ \Delta\boldsymbol{\varepsilon}_i). \tag{42}$$

The inverse of $\mathbf{K}_{11}$ exists since rigid body motions are eliminated by the constraints. Note that $\mathbf{K}_{11}$ possesses a structure as the element matrix $\hat{\mathbf{k}}_e^m$, thus there are zero entries on the main diagonal. This requires a solver which is able to handle such kind of matrices. An eigenvalue analysis of $\mathbf{K}_{11}$ leads in the linear case to 5 or 9 negative eigenvalues depending on the number of used constraints. This is consequence of the Lagrange multiplier approach which leads to a saddle point problem.

With (42) Equation (40) reduces to

$$\delta\bar{\mathbf{V}}_i^{mT}\ \left(\mathbf{K}_i^m\ \Delta\bar{\mathbf{V}}_i^m + \mathbf{F}_i^m\right) = \delta\boldsymbol{\varepsilon}_i^T(\mathbf{D}_i\ \Delta\boldsymbol{\varepsilon}_i + \boldsymbol{\sigma}_i), \tag{43}$$

where

$$\boldsymbol{\sigma}_i = \frac{1}{A_0}(\mathbf{F}_2 - \mathbf{K}_{21}\ \mathbf{K}_{11}^{-1}\ \mathbf{F}_1), \qquad \mathbf{D}_i = \frac{1}{A_0}(\mathbf{K}_{22} - \mathbf{K}_{21}\ \mathbf{K}_{11}^{-1}\ \mathbf{K}_{12}) \tag{44}$$

are the stress resultants and the material matrix at Gauss point i. Finally (43) is inserted into the linearized coupled boundary value problem (35)

$$\mathrm{L}\ [g(\boldsymbol{\theta}^h, \delta\boldsymbol{\theta}^h), \Delta\boldsymbol{\theta}^h] = \sum_{e=1}^{numel}\begin{bmatrix}\delta\mathbf{v}^M\\ \delta\boldsymbol{\varepsilon}_1\\ \vdots\\ \delta\boldsymbol{\varepsilon}_i\\ \vdots\\ \delta\boldsymbol{\varepsilon}_{NGP}\end{bmatrix}_e^T\left\{\begin{bmatrix}\mathbf{k}^M(\mathbf{D}_i) & \mathbf{0} & \vdots & \mathbf{0} & \vdots & \mathbf{0}\\ \mathbf{0} & \mathbf{D}_1 & \vdots & \mathbf{0} & \vdots & \mathbf{0}\\ \cdots & \cdots & \ddots & \mathbf{0} & \cdots & \cdots\\ \mathbf{0} & \mathbf{0} & \mathbf{0} & \mathbf{D}_i & \mathbf{0} & \mathbf{0}\\ \cdots & \cdots & \cdots & \mathbf{0} & \ddots & \cdots\\ \mathbf{0} & \mathbf{0} & \cdots & \mathbf{0} & \cdots & \mathbf{D}_{NGP}\end{bmatrix}_e\begin{bmatrix}\Delta\mathbf{v}^M\\ \Delta\boldsymbol{\varepsilon}_1\\ \vdots\\ \Delta\boldsymbol{\varepsilon}_i\\ \vdots\\ \Delta\boldsymbol{\varepsilon}_{NGP}\end{bmatrix}_e + \begin{bmatrix}\mathbf{f}^M(\boldsymbol{\sigma}_i)\\ \boldsymbol{\sigma}_1\\ \vdots\\ \boldsymbol{\sigma}_i\\ \vdots\\ \boldsymbol{\sigma}_{NGP}\end{bmatrix}_e\right\}. \tag{45}$$

As Equation (45) shows there is coupling between the micro and macro problems. The shell strains $\boldsymbol{\varepsilon}_i$ enter in Equation (38), the stress resultants $\boldsymbol{\sigma}_i$ and the material matrix $\mathbf{D}_i$ according to (44) enter in $\mathbf{f}^M(\boldsymbol{\sigma}_i)$ and $\mathbf{k}^M(\mathbf{D}_i)$, respectively. The coupled nonlinear system of equations is simultaneously solved within the Newton iteration scheme. The iteration is terminated for the actual load step when local equilibrium in all Gauss points is attained along with the global equilibrium of the shell which is formulated through the first row of (35) or (45). The alternative is a nested iteration, where the next global iteration step is not till performed after convergence in all micro problems is attained.

5 | EXTENSION TO FINITE DEFORMATION PROBLEMS

The generalization for finite deformations is obtained with a rewritten form of Equation (27) as

$$\left.\begin{aligned} \mathbf{u} &= \bar{\mathbf{H}}\,\mathbf{X} + \tilde{\mathbf{u}} \\ \tilde{\mathbf{u}}^{+} &= \tilde{\mathbf{u}}^{-} \end{aligned}\right\} \quad \text{at} \quad \begin{aligned} x &= \pm l_x/2, \\ y &= \pm l_y/2, \end{aligned} \tag{46}$$

where $\bar{\mathbf{H}} = \bar{\mathbf{F}} - \mathbf{1}$ is the macroscopic displacement gradient. As we apply the assumed strain interpolation[40] for the transverse shear strains to avoid shear locking in case of thin shells a variational consistent form of the macroscopic deformation gradient $\bar{\mathbf{F}}$ is not available. This follows from the fact that the assumed transverse shear strains γ_α are components of the symmetric macroscopic Green–Lagrange strain tensor $\bar{\mathbf{E}}$ from which $\bar{\mathbf{F}}$ with 9 components cannot be recomputed.

However, it is possible to compute the right stretch tensor $\bar{\mathbf{U}}$ of the polar decomposition $\bar{\mathbf{F}} = \bar{\mathbf{R}}\,\bar{\mathbf{U}}$ with the rotation tensor $\bar{\mathbf{R}}$. The application of $\bar{\mathbf{R}}$ means a rigid body rotation for the RVE and therefore can be omitted. Thus, an alternative to (46) is the loading of the RVE with the strains $\bar{\mathbf{U}} - \mathbf{1}$. The strains $\bar{\mathbf{U}} - \mathbf{1}$ can be computed from $\bar{\mathbf{E}}$, as it is a special case of the generalized strain measures $\bar{\mathbf{E}}^{(k)} = \frac{1}{2\,k}(\bar{\mathbf{C}}^{k} - \mathbf{1})$ with $k = 1/2$. Here, $\bar{\mathbf{C}}$ denotes the macroscopic right Cauchy–Green tensor which can be computed from $\bar{\mathbf{E}}$ via $\bar{\mathbf{C}} = 2\,\bar{\mathbf{E}} + \mathbf{1}$.

For this purpose the shell strains (3) are used to define

$$\bar{\mathbf{E}}^{\varepsilon} = \begin{bmatrix} \varepsilon_{11} & \varepsilon_{12} & \varepsilon_{13} \\ \varepsilon_{21} & \varepsilon_{22} & \varepsilon_{23} \\ \varepsilon_{31} & \varepsilon_{32} & \varepsilon_{33} \end{bmatrix}, \qquad \bar{\mathbf{E}}^{\kappa} = \begin{bmatrix} \kappa_{11} & \kappa_{12} & \kappa_{13} \\ \kappa_{21} & \kappa_{22} & \kappa_{23} \\ \kappa_{31} & \kappa_{32} & \kappa_{33} \end{bmatrix}, \tag{47}$$

where $\varepsilon_{\alpha 3} = \gamma_\alpha/2$, $\varepsilon_{33} = 0$, $\varepsilon_{ij} = \varepsilon_{ji}$ and $\kappa_{i3} = 0$, $\kappa_{ij} = \kappa_{ji}$. With $\bar{\mathbf{E}}^{\varepsilon}$ and $\bar{\mathbf{E}}^{\kappa}$ the generalized shell strains $\bar{\mathbf{E}}^{\varepsilon(k)}$ and $\bar{\mathbf{E}}^{\kappa(k)}$ are computed via Equation (A2) Appendix A. The relevant components of $\bar{\mathbf{E}}^{\varepsilon(k)}$ and $\bar{\mathbf{E}}^{\kappa(k)}$ are arranged in the vector

$$\boldsymbol{\varepsilon}^{(k)} = \left[E_{11}^{\varepsilon(k)}, E_{22}^{\varepsilon(k)}, 2E_{12}^{\varepsilon(k)}, E_{11}^{\kappa(k)}, E_{22}^{\kappa(k)}, 2E_{12}^{\kappa(k)}, 2E_{13}^{\varepsilon(k)}, 2E_{23}^{\varepsilon(k)}\right]^{T}. \tag{48}$$

The vector of generalized stress resultants $\boldsymbol{\sigma}^{(k)}$ is work conjugate to $\boldsymbol{\varepsilon}^{(k)}$. In order to derive the transformation relations between $\boldsymbol{\sigma}^{(k)}$ and $\boldsymbol{\sigma}$ as well as of the associated material matrices we insert $\delta\boldsymbol{\varepsilon}^{(k)} = \mathbf{P}\,\delta\boldsymbol{\varepsilon}$ and $\Delta\boldsymbol{\varepsilon}^{(k)} = \mathbf{P}\,\Delta\boldsymbol{\varepsilon}$ with $\mathbf{P} = \partial_{\boldsymbol{\varepsilon}}\boldsymbol{\varepsilon}^{(k)}$ as well as $\Delta\delta\boldsymbol{\varepsilon}^{(k)}\;\boldsymbol{\sigma}^{(k)} = \delta\boldsymbol{\varepsilon}^{T}\;\mathbf{L}\;\Delta\boldsymbol{\varepsilon}$ into the linearized virtual work per unit area

$$\begin{aligned} \delta\boldsymbol{\varepsilon}^{(k)T}\boldsymbol{\sigma}^{(k)} + \Delta(\delta\boldsymbol{\varepsilon}^{(k)T}\boldsymbol{\sigma}^{(k)}) &= \delta\boldsymbol{\varepsilon}^{(k)T}(\boldsymbol{\sigma}^{(k)} + \mathbf{D}^{(k)}\Delta\boldsymbol{\varepsilon}) + \Delta\delta\boldsymbol{\varepsilon}^{(k)T}\boldsymbol{\sigma}^{(k)} \\ &= \delta\boldsymbol{\varepsilon}^{T}[\mathbf{P}^{T}\boldsymbol{\sigma}^{(k)} + (\mathbf{P}^{T}\mathbf{D}^{(k)}\mathbf{P} + \mathbf{L})\Delta\boldsymbol{\varepsilon}], \end{aligned} \tag{49}$$

where $\mathbf{D}^{(k)} = \partial_{\boldsymbol{\varepsilon}^{(k)}}\boldsymbol{\sigma}^{(k)}$. From (49) one can deduce the transformation relations of the stress resultants and the material matrix. They read

$$\boldsymbol{\sigma} = \mathbf{P}^{T}\boldsymbol{\sigma}^{(k)}, \qquad \mathbf{D} = \mathbf{P}^{T}\;\mathbf{D}^{(k)}\;\mathbf{P} + \mathbf{L}, \tag{50}$$

where $\mathbf{P}$ and $\mathbf{L}$ are specified as follows. The component representation of $\delta\boldsymbol{\varepsilon}^{(k)} = \mathbf{P}\;\delta\boldsymbol{\varepsilon}$ reads

$$\begin{bmatrix} \delta\varepsilon_{11}^{(k)} \\ \delta\varepsilon_{22}^{(k)} \\ 2\delta\varepsilon_{12}^{(k)} \\ \delta\kappa_{11}^{(k)} \\ \delta\kappa_{22}^{(k)} \\ 2\delta\kappa_{12}^{(k)} \\ \delta\gamma_{1}^{(k)} \\ \delta\gamma_{2}^{(k)} \end{bmatrix} = \begin{bmatrix} P_{11}^{\varepsilon} & P_{12}^{\varepsilon} & P_{14}^{\varepsilon} & 0 & 0 & 0 & P_{15}^{\varepsilon} & P_{16}^{\varepsilon} \\ P_{21}^{\varepsilon} & P_{22}^{\varepsilon} & P_{24}^{\varepsilon} & 0 & 0 & 0 & P_{25}^{\varepsilon} & P_{26}^{\varepsilon} \\ P_{41}^{\varepsilon} & P_{42}^{\varepsilon} & P_{44}^{\varepsilon} & 0 & 0 & 0 & P_{45}^{\varepsilon} & P_{46}^{\varepsilon} \\ 0 & 0 & 0 & P_{11}^{\kappa} & P_{12}^{\kappa} & P_{14}^{\kappa} & 0 & 0 \\ 0 & 0 & 0 & P_{21}^{\kappa} & P_{22}^{\kappa} & P_{24}^{\kappa} & 0 & 0 \\ 0 & 0 & 0 & P_{41}^{\kappa} & P_{42}^{\kappa} & P_{44}^{\kappa} & 0 & 0 \\ P_{51}^{\varepsilon} & P_{52}^{\varepsilon} & P_{54}^{\varepsilon} & 0 & 0 & 0 & P_{55}^{\varepsilon} & P_{56}^{\varepsilon} \\ P_{61}^{\varepsilon} & P_{62}^{\varepsilon} & P_{63}^{\varepsilon} & 0 & 0 & 0 & P_{65}^{\varepsilon} & P_{66}^{\varepsilon} \end{bmatrix} \begin{bmatrix} \delta\varepsilon_{11} \\ \delta\varepsilon_{22} \\ 2\delta\varepsilon_{12} \\ \delta\kappa_{11} \\ \delta\kappa_{22} \\ 2\delta\kappa_{12} \\ \delta\gamma_{1} \\ \delta\gamma_{2} \end{bmatrix}, \tag{51}$$

TABLE 2 Large strain transformations at a Gauss point i on macro level.

1. Compute generalized shell strains $\boldsymbol{\varepsilon}^{(k)}$ with $k = 1/2$ according to Equation (48)

$$\boldsymbol{\varepsilon}^{(k)} = [E_{11}^{\varepsilon(k)}, E_{22}^{\varepsilon(k)}, 2E_{12}^{\varepsilon(k)}, E_{11}^{\kappa(k)}, E_{22}^{\kappa(k)}, 2E_{12}^{\kappa(k)}, 2E_{13}^{\varepsilon(k)}, 2E_{23}^{\varepsilon(k)}]^T$$

2. Apply the generalized strains $\bar{\mathbf{E}}^{(k)}$ to the RVE with $\boldsymbol{\varepsilon}^{(k)}$ in Equation (32)

$$\mathbf{u}^+ = \mathbf{u}^- + \bar{\mathbf{E}}^{(k)} \Delta \mathbf{X}$$

Compute generalized stress resultants $\boldsymbol{\sigma}^{(k)}$ and material matrix $\mathbf{D}^{(k)}$ via Equation (44)

$$\boldsymbol{\sigma}^{(k)} = \frac{1}{A_0}(\mathbf{F}_2 - \mathbf{K}_{12}^T \mathbf{K}_{11}^{-1} \mathbf{F}_1) \qquad \mathbf{D}^{(k)} = \frac{1}{A_0}(\mathbf{K}_{22} - \mathbf{K}_{12}^T \mathbf{K}_{11}^{-1} \mathbf{K}_{12})$$

3. Transform $\boldsymbol{\sigma}^{(k)}$ and $\mathbf{D}^{(k)}$ according to Equation (50)

$$\boldsymbol{\sigma} = \mathbf{P}^T \boldsymbol{\sigma}^{(k)} \qquad \mathbf{D} = \mathbf{P}^T \mathbf{D}^{(k)} \mathbf{P} + \mathbf{L}$$

and obtain $\boldsymbol{\sigma}$ and $\mathbf{D}$ for use in the element matrices Equation (36).

where P_{ij}^{ε} and P_{ij}^{κ} are computed with $\bar{\mathbf{E}}^{\varepsilon}$ and $\bar{\mathbf{E}}^{\kappa}$ via Equation (A7) in Appendix A, respectively. Due to $\bar{E}_{33} = \bar{E}_{33}^{(k)} = 0$ the components $\hat{P}_{i3}^{\varepsilon} = \hat{P}_{3i}^{\varepsilon}$ and $\hat{P}_{i3}^{\kappa} = \hat{P}_{3i}^{\kappa}$ have not to be taken into account.

The component representation of the term $\Delta\delta\boldsymbol{\varepsilon}^{(k)T}\boldsymbol{\sigma}^{(k)} = \delta\boldsymbol{\varepsilon}^T \mathbf{L} \Delta\boldsymbol{\varepsilon}$ reads

$$\Delta\delta\boldsymbol{\varepsilon}^{(k)T}\boldsymbol{\sigma}^{(k)} = \begin{bmatrix} \delta\varepsilon_{11} \\ \delta\varepsilon_{22} \\ 2\delta\varepsilon_{12} \\ \delta\kappa_{11} \\ \delta\kappa_{22} \\ 2\delta\kappa_{12} \\ \delta\gamma_1 \\ \delta\gamma_2 \end{bmatrix}^T \begin{bmatrix} L_{11}^{\varepsilon} & L_{12}^{\varepsilon} & L_{14}^{\varepsilon} & 0 & 0 & 0 & L_{15}^{\varepsilon} & L_{16}^{\varepsilon} \\ L_{21}^{\varepsilon} & L_{22}^{\varepsilon} & L_{24}^{\varepsilon} & 0 & 0 & 0 & L_{25}^{\varepsilon} & L_{26}^{\varepsilon} \\ L_{41}^{\varepsilon} & L_{42}^{\varepsilon} & L_{44}^{\varepsilon} & 0 & 0 & 0 & L_{45}^{\varepsilon} & L_{46}^{\varepsilon} \\ 0 & 0 & 0 & L_{11}^{\kappa} & L_{12}^{\kappa} & L_{14}^{\kappa} & 0 & 0 \\ 0 & 0 & 0 & L_{21}^{\kappa} & L_{22}^{\kappa} & L_{24}^{\kappa} & 0 & 0 \\ 0 & 0 & 0 & L_{41}^{\kappa} & L_{42}^{\kappa} & L_{44}^{\kappa} & 0 & 0 \\ L_{51}^{\varepsilon} & L_{52}^{\varepsilon} & L_{54}^{\varepsilon} & 0 & 0 & 0 & L_{55}^{\varepsilon} & L_{56}^{\varepsilon} \\ L_{61}^{\varepsilon} & L_{62}^{\varepsilon} & L_{63}^{\varepsilon} & 0 & 0 & 0 & L_{65}^{\varepsilon} & L_{66}^{\varepsilon} \end{bmatrix} \begin{bmatrix} \Delta\varepsilon_{11} \\ \Delta\varepsilon_{22} \\ 2\Delta\varepsilon_{12} \\ \Delta\kappa_{11} \\ \Delta\kappa_{22} \\ 2\Delta\kappa_{12} \\ \Delta\gamma_1 \\ \Delta\gamma_2 \end{bmatrix}, \tag{52}$$

where L_{ij}^{ε} and L_{ij}^{κ} are computed using $\bar{\mathbf{E}}^{\varepsilon}$ and $\bar{\mathbf{E}}^{\kappa}$ via Equation (A8) along with (A9)–(A12) in Appendix A. Again, due to $\bar{E}_{33} = \bar{E}_{33}^{(k)} = 0$ the components $L_{i3}^{\varepsilon} = L_{3i}^{\varepsilon}$ and $L_{i3}^{\kappa} = L_{3i}^{\kappa}$ have not to be taken into account.

Numerical computations show that in many cases, especially for thin shells, curvatures are not the source for large strains. Hence it is possible to perform the transformations only for the membrane and shear terms. In that case $E_{\alpha\beta}^{\kappa(k)}$ in (48) has to be replaced by $\kappa_{\alpha\beta}$. and thereby it follows $P_{ij}^{\kappa} = \delta_{ij}$, $L_{ij}^{\kappa} = 0$. The shear terms could be handled in an analogues way, as usually the transverse shear strains are also small.

Finally we summarize the necessary transformations for large deformations in Table 2. The steps 1 and 3 are not applicable in case of small strains. If so it holds $\boldsymbol{\varepsilon}^{(k)} = \boldsymbol{\varepsilon}$, hereby $\bar{\mathbf{E}}^{(k)} = \bar{\mathbf{E}}$ as well as $\boldsymbol{\sigma} = \boldsymbol{\sigma}^{(k)}$ and $\mathbf{D} = \mathbf{D}^{(k)}$.

> *Remark.* The constraints in Section 3.1 avoiding the length dependency of the transverse shear stiffness are formulated under the assumption of geometrical linearity. Our numerical investigations show that this is admissible also for problems which require a geometrical nonlinear computation. In case of nonlinear elasticity or inelasticity Equation (12) has to be replaced by the corresponding relation for the linearized stresses. To maintain quadratic convergence in the Newton iteration process constant values for C_{ij} , $1 \le i,j \le 6$ of the last load step are taken.

Furthermore, it is important to note that functional (5) does not hold for inelastic problems, whereas variational Equation (6) and the successive ones are applicable. Hence the stresses $\mathbf{S}$ of the micro problem are computed using the respective inelastic material law.

6 | EXAMPLES

The developed model has been implemented in an extended version of the general finite element program FEAP.[41] With the first example we compare for a homogeneous RVE the finite element solutions with analytical results. The second

example is concerned with a layered RVE with different elasticity constants for the layers. Furthermore, several coupled micro–macro shell problems are investigated. Comparisons are given with full scale solutions computed with 27-noded brick elements as well as with 8-noded solid shell elements.[42,43] The solid shell elements possess an orientation which has to be considered when generating the meshes. For the present examples the thickness direction of the elements must coincide with the z–direction of the shell and the RVE. The element[42] is used here with assumed transverse shear strain interpolation (ANS) and 5 EAS parameters. The solid shell element[43] is based on a Hu–Washizu variational formulation. Note, that element matrix (25) requires two or three additional nodes for the Lagrange parameters. In the following we do not explicitly point out the extra nodes when describing the RVE discretizations.

6.1 | Homogeneous linear elastic isotropic RVE

With the first example we consider a homogeneous RVE with $l_x = l_y = l = h = 2$ mm. It is important to show that the developed homogenization method yields the material matrix of the Reissner–Mindlin shell theory

$$\mathbf{D} = \int_{h^-}^{h^+} \mathbf{A}^T \mathbb{C}\, \mathbf{A}\, \mathrm{d}z, \qquad \mathbf{A} = \begin{bmatrix} \mathbf{1}_3 & z\,\mathbf{1}_3 & \mathbf{0} \\ \mathbf{0} & \mathbf{0} & \mathbf{1}_2 \end{bmatrix}, \qquad \mathbb{C} = \begin{bmatrix} \mathbb{C}_m & \mathbf{0} \\ \mathbf{0} & \mathbb{C}_s \end{bmatrix},$$
$$\mathbf{D} = \begin{bmatrix} \mathbf{D}_m & \mathbf{D}_{mb} & \mathbf{0} \\ \mathbf{D}_{mb} & \mathbf{D}_b & \mathbf{0} \\ \mathbf{0} & \mathbf{0} & \mathbf{D}_s \end{bmatrix}. \tag{53}$$

The indices m, b, s of the submatrices refer to membrane, bending and shear, respectively. Furthermore, $\mathbf{1}_n$ denotes a unit matrix of order n. For linear elastic isotropic material behavior it holds

$$\mathbb{C}_m = \frac{E}{1-\nu^2} \begin{bmatrix} 1 & \nu & 0 \\ \nu & 1 & 0 \\ 0 & 0 & \frac{1-\nu}{2} \end{bmatrix}, \qquad \mathbb{C}_s = G \begin{bmatrix} 1 & 0 \\ 0 & 1 \end{bmatrix}, \qquad G = \frac{E}{2\,(1+\nu)}. \tag{54}$$

We choose Young's modulus $E = 10^5$ N/mm^2 and Poisson's ratio $\nu = 0.4$ as elasticity data.

6.1.1 | Mid-surface as reference surface

Choosing the mid–surface as reference surface, thus $h^- = -h/2$, $h^+ = h/2$, the integration of the submatrices in Equation (53) leads to

$$\mathbf{D}_m = h\, \mathbb{C}_m, \qquad \mathbf{D}_{mb} = \mathbf{0},$$
$$\mathbf{D}_b = \frac{h^3}{12}\, \mathbb{C}_m, \qquad \mathbf{D}_s = \kappa\, h\, \mathbb{C}_s, \tag{55}$$

where the shear stiffness is corrected by the factor κ. For this purpose Reissner[44] derived the value $\kappa = 5/6$. The finite element solutions must display the correct structure of $\mathbf{D}$ with decoupling of the submatrices for membrane, bending and transverse shear deformations. As an example, pure bending of a homogeneous plate or shell would deliver besides bending moments also to membrane and shear forces, if the correct structure of $\mathbf{D}$ is not existent.

For the finite element solutions we use hexahedral elements with 27 or 64 nodes. Evaluation of Equation $(44)_2$ yields exactly the zero entries in Equations (53) and (55) for all meshes starting with a $1 \times 1 \times 1$ discretization. The nonzero values in $\mathbf{D}_m$ and $\mathbf{D}_b$ are exact for any ratio l/h and any mesh density starting with a $1 \times 1 \times 1$ mesh.

Furthermore, the 64-node element yields exact values for the shear stiffness. The shear correction factor $\kappa = 5/6$ is obtained for any mesh density with 5 or 9 constraints according to Section 3.1, see Table 3. Using the 27-node element 2×2 or 1 element in-plane are sufficient for 9 or 5 constraints, respectively. In thickness direction mesh refinement is necessary to obtain convergence against the value $\kappa = 5/6$, see Table 4.

TABLE 3 Shear correction factor κ using the 3D or 2D material law in the constraints.

Mesh (64-node elements)	1 × 1 × 1	2 × 2 × 2	3 × 3 × 3	4 × 4 × 4	5 × 5 × 5
9 constraints with 3D material constants C_{ij}	0.83333	0.83333	0.83333	0.83333	0.83333
5 constraints with 2D material constants $\bar{C}_{ij}$	0.83333	0.83333	0.83333	0.83333	0.83333

TABLE 4 Convergence of the shear correction factor κ using 27-node elements.

Mesh (27-node elements)	2 × 2 × 1	2 × 2 × 2	2 × 2 × 4	2 × 2 × 8	2 × 2 × 16
9 constraints with 3D material constants C_{ij}	1.00000	0.84210	0.83387	0.83336	0.83333
Mesh (27-node elements)	**1 × 1 × 1**	**1 × 1 × 2**	**1 × 1 × 4**	**1 × 1 × 8**	**1 × 1 × 16**
5 constraints with 2D material constants $\bar{C}_{ij}$	1.00000	0.84210	0.83387	0.83336	0.83333

TABLE 5 Shear correction factor κ for different ratio l/h computed with one 64-node element.

l/h	0.01	0.1	1	10	100
κ	0.83333	0.83333	0.83333	0.83333	0.83333

Next a variation of the length ratio l/h is performed with one 64-node element. Table 5 shows that κ is independent of l/h. The same holds when using a mesh of 27–node elements. This proves that the length dependency of the shear stiffness as is discussed in Section 3.1 is effectively removed with the constraints (18).

Figure 3 shows for an applied shell shear strain $\gamma_x = 10^{-3}$ and two different length to thickness ratios the quadratic distribution of the transverse shear stresses through the thickness. The zero stress boundary conditions at the top and bottom surfaces are approximately fulfilled. Furthermore, one can see that the results are independent of l/h. The other stress components are identically zero. This means that a pure shear stress state is obtained. There are no inadmissible bending deformations. When using the 64–node element with cubic shape functions the shear stresses are exact zero at the top and bottom surfaces. The analytical solution reads

$$\sigma_{xz} = 1.5\ \kappa\ G\ \gamma_x\ [1 - (2z/h)^2] = 44.64\ [1 - (2z/h)^2] \qquad [\mathrm{N/mm^2}]. \tag{56}$$

One 64–node element is sufficient to obtain the correct quadratic shape of the shear stresses, see Figure 4.

6.1.2 | Bottom surface as reference surface

We choose a reference surface at the bottom of the RVE, thus $h^- = 0$ and $h^+ = h$. The submatrices of $\mathbf{D}$ according to (53) are given as follows. The membrane stiffness $\mathbf{D}_m$ and the shear stiffness $\mathbf{D}_s$ correspond to Equation (55), whereas the bending stiffness and the coupling matrix become

$$\mathbf{D}_b = \frac{h^3}{3}\mathbb{C}_m, \qquad \mathbf{D}_{mb} = \frac{h^2}{2}\mathbb{C}_m. \tag{57}$$

Again we compute the finite element solutions by evaluation of Equation $(44)_2$. The results agree with the analytical solution for any ratio l/h and any mesh density. The results for the shear terms correspond to those of Section 6.1.1.

6.2 | RVE with three linear elastic isotropic layers

We consider a RVE with three linear elastic layers according to Figure 5, see also Reference 29. The x, y, z–coordinate system is placed at the center of the bloc. The external dimensions of the RVE are $l_x = l_y = h = 20$ cm. We emphasize that the results for all stiffness values are independent of l_x and l_y. The heights of the individual layers depend on the

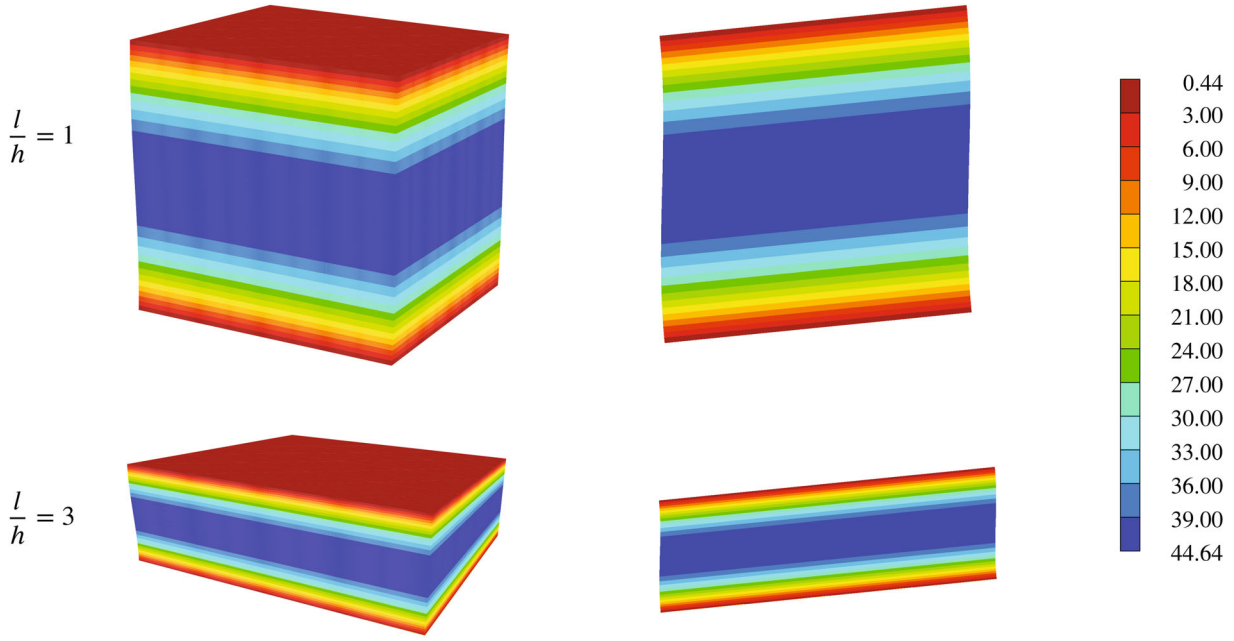

FIGURE 3 Shear stresses σ_{xz} of the homogeneous RVE in N/mm^2 for two different length to thickness ratios, the deformations are amplified by a factor 100.

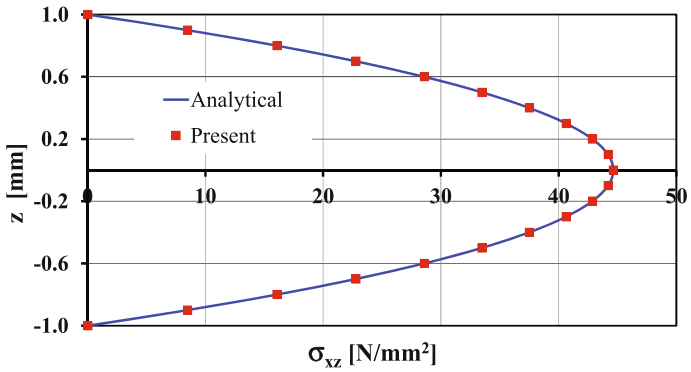

FIGURE 4 Shear stresses σ_{xz} of the homogeneous RVE for a shear strain $\gamma_x = 10^{-3}$.

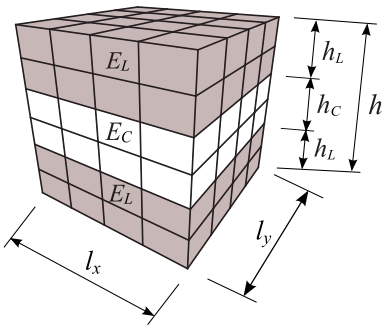

FIGURE 5 Linear elastic isotropic RVE with three layers.

core fraction ρ_C. It holds $h_C = \rho_C\, h$ and $h_L = (1-\rho_c)\, h/2$, thus $h = 2\, h_L + h_C$. Regarding the material parameters, the factor α is introduced to describe the ratio between the stiffness of the core and the outer layers as $\alpha = E_C/E_L$. Here, $E_L = 1000$ kN/cm^2 is Young's modulus of the face layers and $E_C = \alpha\, E_L$ the one of the core. Poisson's ratio $\nu = 0.3$ is constant for the three layers.

Analytical thickness integration in Equation (53) along with summation over the three layers yields exact reference values for the submatrices $\mathbf{D}_m$, $\mathbf{D}_b$ and $\mathbf{D}_{mb} = \mathbf{0}$. For the shear correction factor κ an analytical solution has been derived[45]

$$\kappa = \frac{4}{9}\,\frac{T_1^2}{T_2\; T_4} \tag{58}$$

with

$$\begin{aligned}
T_1(\rho_C) &= (1-\rho_C^3) + \rho_C^3\;\alpha,\\
T_2(\rho_C) &= \frac{(1-\rho_C)}{\alpha} + \rho_C,\\
T_3(\rho_C) &= (1-\rho_C^2)^2 + \frac{8}{15}\alpha^2\rho_C^4 + \frac{4}{3}\alpha\rho_C^2(1-\rho_C^2),\\
T_4(\rho_C) &= A(\rho_C)\;\alpha + \rho_C\; T_3,\\
A(\rho_C) &= \frac{(1-\rho_C)^3}{15}\;(3\rho_C^2 + 9\rho_C + 8).
\end{aligned} \tag{59}$$

For the finite element solution each layer is discretized with one 64-node element. Evaluation of Equation $(44)_2$ yields the material matrix $\mathbf{D}$. The submatrices for membrane and bending agree exact with the analytical solution for any stiffness ratio α and core fraction ρ_C. Here, we focus on the shear stiffness matrix $\mathbf{D}_s = D_s\,\mathbf{1}_2$. From this follows the finite element solution $\kappa = D_s/\bar{D}_s$ with $\bar{D}_s = (2E_L\; h_L + E_C\; h_C)/2\;(1+\nu)$. A variation of the core fraction ρ_c and of the stiffness ratio α is performed. The excellent agreement with the analytical solution can be seen in Figure 6. For $\alpha \ll 1$ the weak core leads to a drastic reduction of the shear stiffness. The minimum shear correction factor for $\alpha = 0.001$ is $\kappa = 0.0023$. When replacing C_{ij} in the constraints (18) by δ_{ij} (Kronecker–Delta) one obtains the broken lines, see also fig. 10 in Reference 30, fig. 12 in Reference 32. Hence, the differences to the analytical solution amount up to 16.9%. When using element formulation[46] one obtains with deviations of less than 10^{-10} % practically the analytical solution. Applying a strain $\gamma_x = 10^{-3}$ to the RVE the distribution of the shear strains are shown for a stiffness ratio $\alpha = 0.001$ and two different core fractions ρ_C in Figure 7. It is obvious that displacement boundary conditions would restrain the extreme shear deformations in the thin central layer. The results of this example using 5 or 9 Lagrange parameters agree with each other. The following examples are computed only with 5 Lagrange parameters as this means less effort in comparison with the 9-parameter version.

6.3 | Clamped layered beam

Present example has been taken from Reference 35. A cantilever with a nonsymmetric cross-ply laminate is shown in Figure 8. The stacking sequence for the 10 layers reads $[90°/0°]_5$, where 0° coincides with the length direction of the beam. The geometrical data as well as the elasticity parameters for transversal isotropy along with the chosen mesh densities are given in Figure 8. A right-handed x, y, z–coordinate system is placed at the clamped edge of the beam, where x and z coincide with the length direction and the thickness direction, respectively. Hence, the beam occupies the space $0 \le x \le L$, $-b/2 \le y \le b/2$ and $-h/2 \le z \le h/2$. The load $F = 175$ N is applied as a line load $\bar{q} = F/b$ in the FE2 plate model and as a surface load $\bar{p} = F/(b \cdot h)$ in the 3D reference model. The RVE length is chosen as $l_x = l_y = h$. It is ascertained that the results are independent of l_x and l_y.

A geometrical linear analysis is performed. The stresses σ_x and σ_{xz} are computed at the center of the beam using present FE2 model. Refinement of the plate mesh does not alter the results, thus with the 21×1 mesh we obtain the converged solution. A 3D reference solution is obtained with a sufficient fine mesh of solid shell elements.[42] In Figure 9 the stresses are plotted in dependence of the normalized thickness coordinate. The diagrams show conformance of the FE2 solution with the 3D reference solution. The integral of the FE2 shear stresses $\int_{-h/2}^{-h/2} \sigma_{xz}\; \mathrm{d}z$ yields the value 8.74986 N/mm which is practically equal to the shear force $q = F/b = 8.75$ N/mm. A purely parabolic distribution of the transverse shear stresses is obtained in Reference 35.

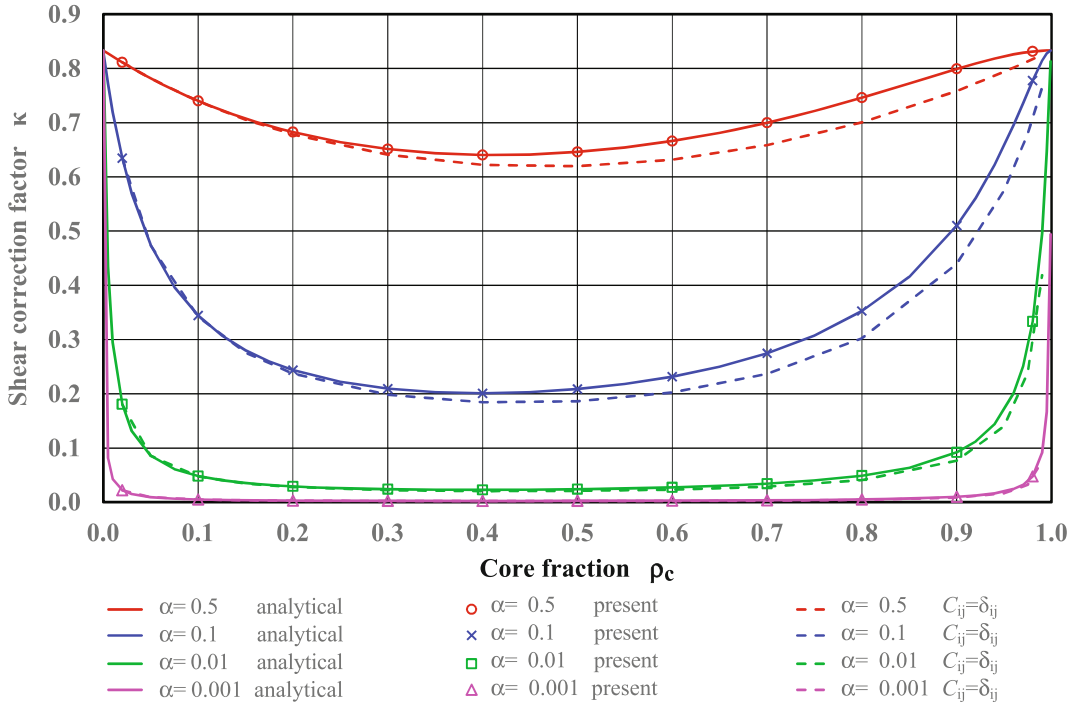

FIGURE 6 Shear correction factors for the linear elastic isotropic RVE with three layers.

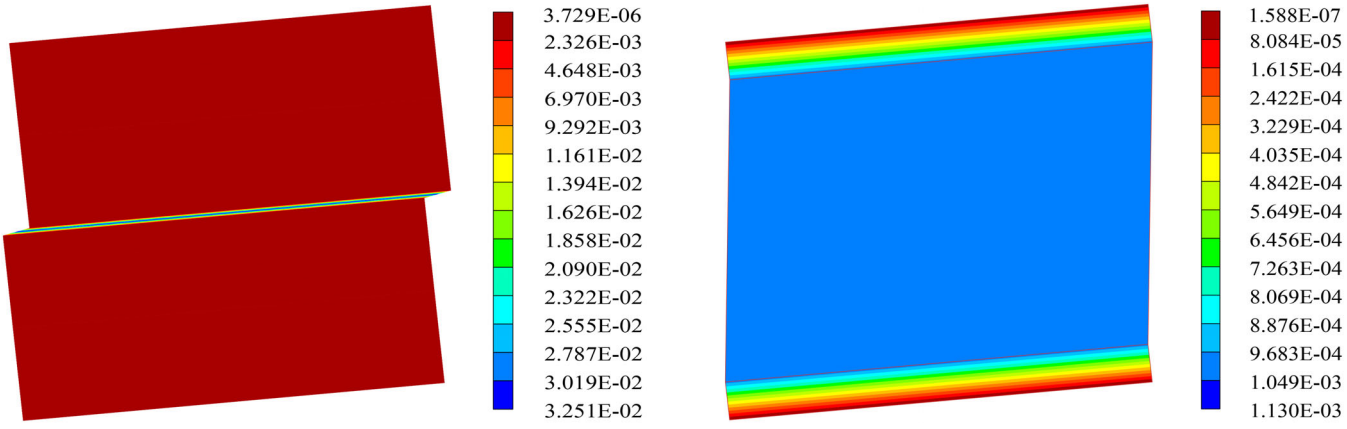

FIGURE 7 Shear strains [-] of the RVE for $\rho_C = 0.02$ (left) and $\rho_C = 0.8$ (right), the deformations are amplified by a factor 100.

6.4 | Layered cylindrical shell

Figure 10 shows a quarter of a cylindrical fiber reinforced composite shell with boundary conditions, loading, geometrical data and mesh densities. The fiber angles for the three layers of equal thickness are [90°/0°/90°], where 0° refers to the circumferential direction and 90° to the length direction of the cylinder. The material constants for transversal isotropy are chosen as

$$\begin{aligned} E_1 &= 125{,}000\ \text{N/mm}^2, & G_{12} &= 4800\ \text{N/mm}^2, \\ E_2 &= 7400\ \text{N/mm}^2, & G_{23} &= 2700\ \text{N/mm}^2, \\ \nu_{12} &= 0.34\ , \end{aligned} \tag{60}$$

where the index 1 refers to the preferred direction of the material.

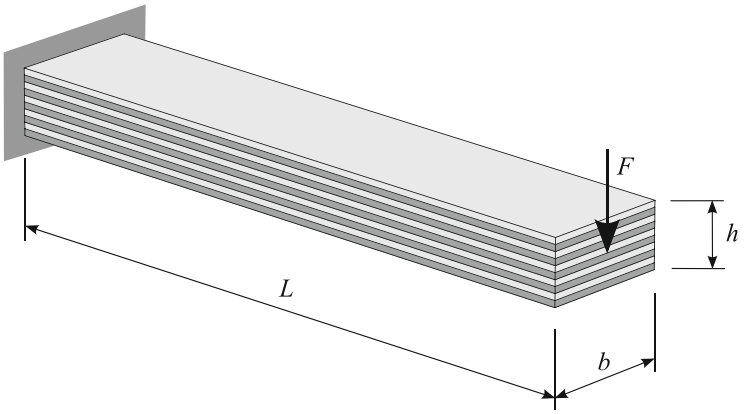

geometrical data:

$L = 100$ mm
$b = 20$ mm
$h = 10$ mm

material data:

$E_1 = 120000$ N/mm^2
$E_2 = 10500$ N/mm^2
$G_{12} = 5250$ N/mm^2
$\nu_{12} = 0.3$
$\nu_{23} = 0.51$

mesh densities:

Plate: 21×1
RVE: one 64-node element per layer
3D: $51 \times 1 \times (10 \times 10)$ (10 elements per layer)

FIGURE 8 Clamped layered beam: geometrical and material data, mesh densities.

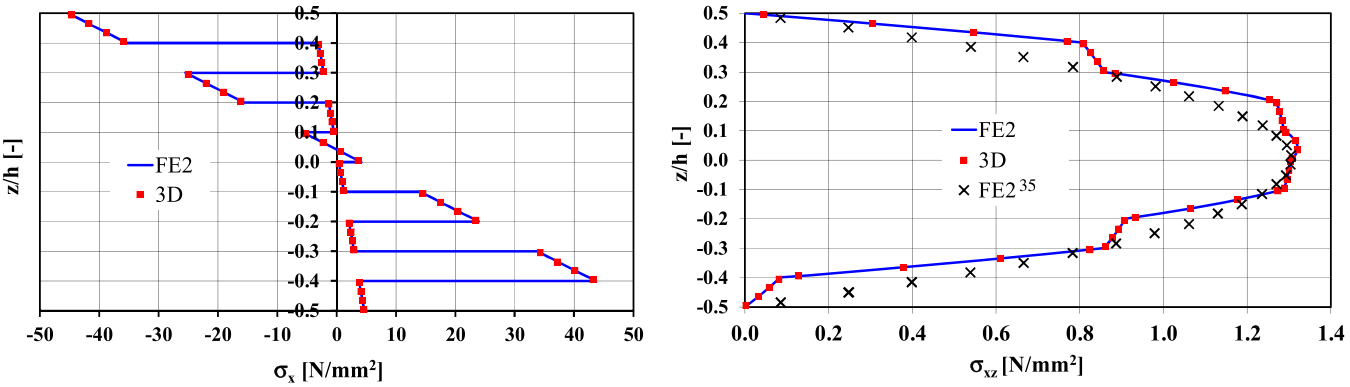

FIGURE 9 Clamped layered beam: Stresses σ_x (left) and σ_{xz} (right) at the center of the beam.

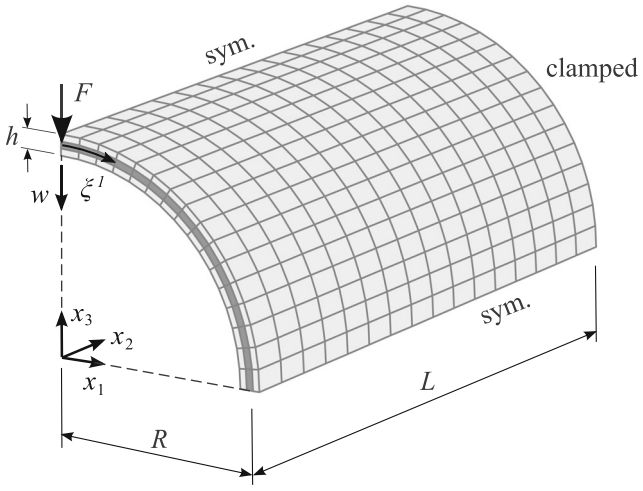

Geometrical data:

$L = 300$ mm
$R = 100$ mm
$h = 1$ mm

Mesh densities:

Shell $n \times n$
3D $n \times n \times (4 + 4 + 4)$
$n = 16, 32, 64$

FIGURE 10 Layered cylindrical shell (not to scale): geometrical data and mesh densities.

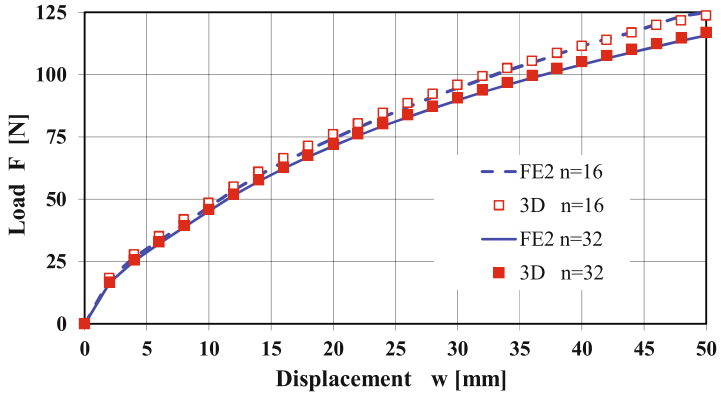

FIGURE 11 Layered cylindrical shell: load F versus displacement w.

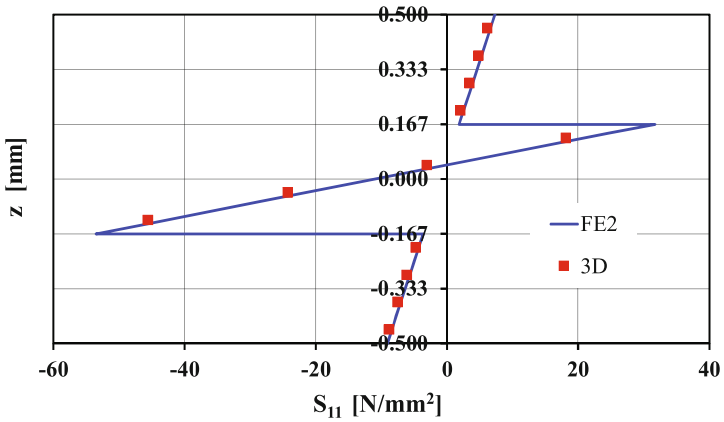

FIGURE 12 Layered cylindrical shell: stress $S_{11}\left(\xi_p^1, \xi_p^2, z\right)$.

The RVE measurements are chosen as $l_x = l_y = h$. It is discretized with one 64–node element for each layer. Reference solutions are computed using solid shell element[42] applying a sufficient fine discretization in thickness direction. The computations are carried out displacement controlled, thus F is computed as reaction for prescribed displacements w with a step size $\Delta w = 2$ mm. We compare the 3D reference solution with results of present two–scale model. The curves in Figure 11 show good agreement between the different models. The results for the mesh with $n = 64$ are not depicted as there are virtually no differences in comparison to $n = 32$. There is virtually no difference between a geometrically linear and nonlinear computation of the RVE. The large strain transformations according to Table 2 have no influence on the results and thereby can be omitted. This follows from the fact that the shell is thin and therefore undergoes only small strains for this type of loading.

For the final configuration ($w = 50$ mm) the Second Piola–Kirchhoff stresses S_{11} and S_{13} at a point P of the reference surface with coordinates $\xi_p^1 = (17/64 \cdot \pi/2) \cdot R$ and $\xi_p^2 = x_{2p} = 7/64 \cdot L$ are displayed in Figures 12 and 13 in dependence of the thickness coordinate $z = \xi^3$. In all diagrams there is good agreement of present FE2 solution with the 3D reference solution. A plot of the deformed configuration is shown in Figure 14.

6.5 | Cylindrical shell subjected to large strains

Present example corresponds to the last one except thickness h, loading and material law. Additionally to the concentrated force F a distributed tension load p is applied at the mid surface in negative x_2-direction at $x_2 = 0$. In this way the structure undergoes large strains. For the reference solution using solid shell elements[43] F is distributed as a line load $f = F/h$ and p as a surface load $q = p/h$ through the thickness (Figure 15). A Neo–Hookean strain energy function $W(\mathbf{C}) = \frac{\mu}{2}(\text{tr } \mathbf{C} -$

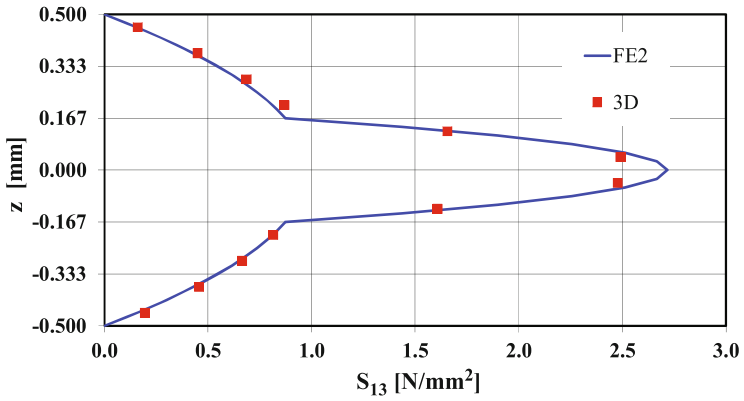

FIGURE 13 Layered cylindrical shell: stress $S_{13}\left(\xi_p^1, \xi_p^2, z\right)$.

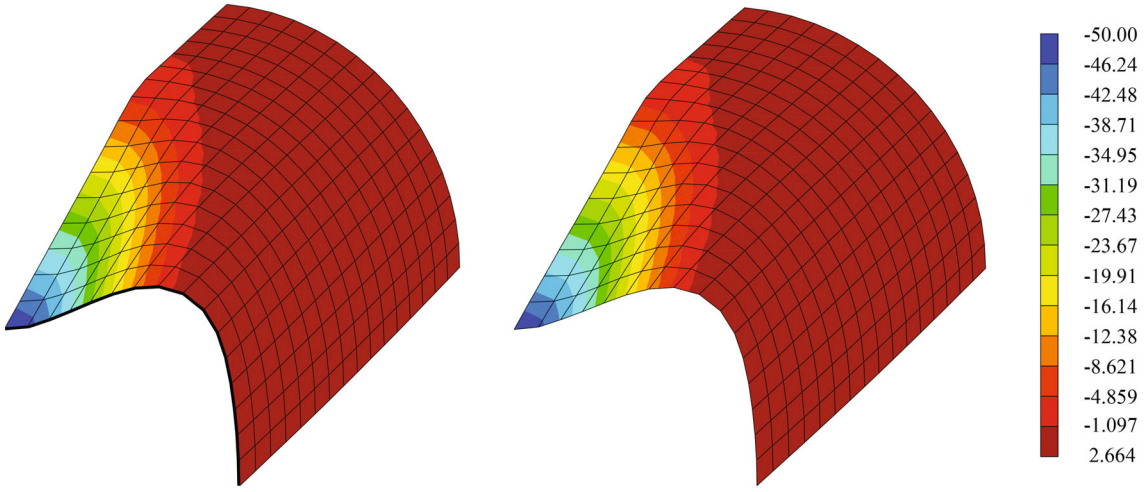

FIGURE 14 Layered cylindrical shell: displacement u_3 (mm) (left: 3D, right: FE2).

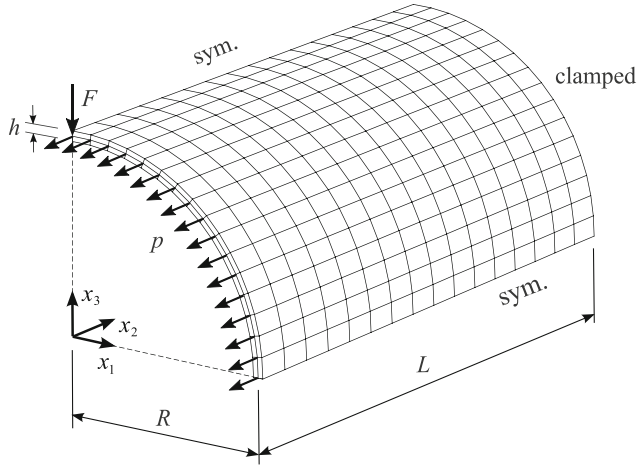

Geometrical data:

$L = 300$ mm
$R = 100$ mm
$h = 5$ mm

Mesh densities:

Shell	$n \times n$
3D	$n \times n \times 4$
	$n = 16, 32$

FIGURE 15 Cylindrical shell with a $16 \times 16 \times 2$ mesh.

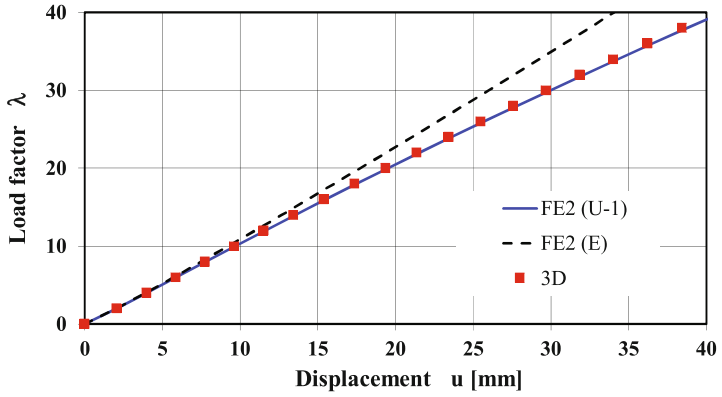

FIGURE 16 Cylindrical shell: load factor λ versus displacement u.

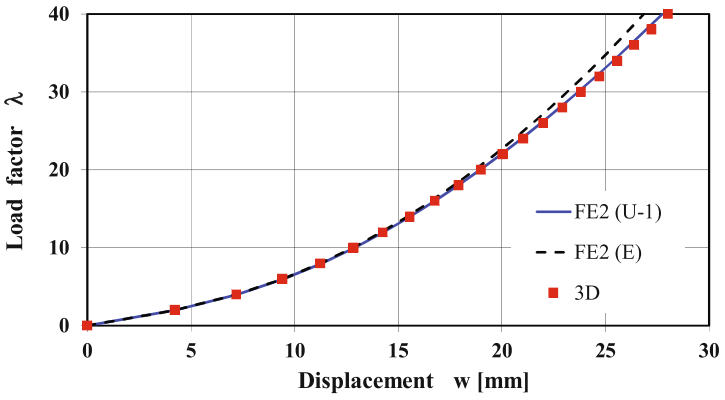

FIGURE 17 Cylindrical shell: load factor λ versus displacement w.

3) + $\frac{\Lambda}{4}$(det $\mathbf{C}$ − 1 − ln (det $\mathbf{C}$))) with compressible part and constants $\mu = 2.1125$ N/mm^2 as well as $\Lambda = 1000$ N/mm^2 is chosen. With $\Lambda \gg \mu$ a quasi-incompressible material behavior is considered. Proportional loading is applied with $F = \lambda\, F_0, p = \lambda\, p_0$, where λ is the load factor and $F_0 = 0.25$ N as well as $p_0 = 0.1$ N/mm. The RVE measurements are chosen as $l_x = l_y = h$. It is discretized using a $1 \times 1 \times 4$ mesh of 8-noded solid shell elements[43] and 8-noded elements for the constraints.

The load deflection curves are computed load controlled with an increase of the load factor λ. They are shown in Figures 16 and 17 with $u = -u_2(0, 0, R)$ as well as $w = -u_3(0, 0, R)$. With $n = 32$ converged solutions are obtained. There is very good agreement of present FE2 solution with the 3D reference solution when the large strain transformations (U-1) according to Table 2 are applied. Without the transformations the RVEs are loaded with the macroscopic Green–Lagrange strains (E) and one obtains the dotted lines. Agreement with the reference solution can only be attained in the range of small deformations where $u \lesssim 10$ mm and $w \lesssim 15$ mm. With increasing strains the deviations are not negligible any more. It should be noted that in present case the curvatures are not the source for large strains. For this reason it is sufficient to apply the large strain transformations only to the membrane and shear part. In so doing one obtains virtually the same results in comparison with the transformation of all components.

The convergence behavior of the Newton scheme is depicted in Table 6 when applying the simultaneous iteration in comparison to a nested iteration. Within the load steps $\lambda = 16 \rightarrow 18$ and $\lambda = 18 \rightarrow 20$ the norm of the global residual vector $|\mathbf{F}|$ is shown for each iteration. Both procedures show quadratic convergence and require the same number of iterations, however the nested iteration additionally needs 3 to 5 local iterations in each global iteration step. The number of local iterations is determined at the Gauss point closest to the concentrated force. For the considered load steps this means a save of computing time of approximately 70%. The iteration behavior in the other load steps is similar.

Contour plots of the displacements u_3 are plotted with respect to the final deformed configuration in Figure 18.

TABLE 6 Iteration behavior for simultaneous and nested iteration.

Load step	Iteration	Simultaneous iteration |F|	Number of local iterations	Nested iteration |F|	Number of local iterations
$\lambda = 16 \rightarrow 18$	1	5.54E+00	1	5.53E+00	3
	2	2.31E−01	1	2.27E−01	5
	3	4.27E−03	1	1.27E−03	4
	4	2.74E−05	1	1.56E−05	3
	5	3.24E−07	1	1.86E−07	3
$\lambda = 18 \rightarrow 20$	1	5.53E+00	1	5.53E+00	3
	2	2.21E−01	1	2.18E−01	5
	3	4.05E−03	1	1.46E−03	4
	4	3.39E−05	1	1.95E−05	3
	5	4.37E−07	1	2.52E−07	3

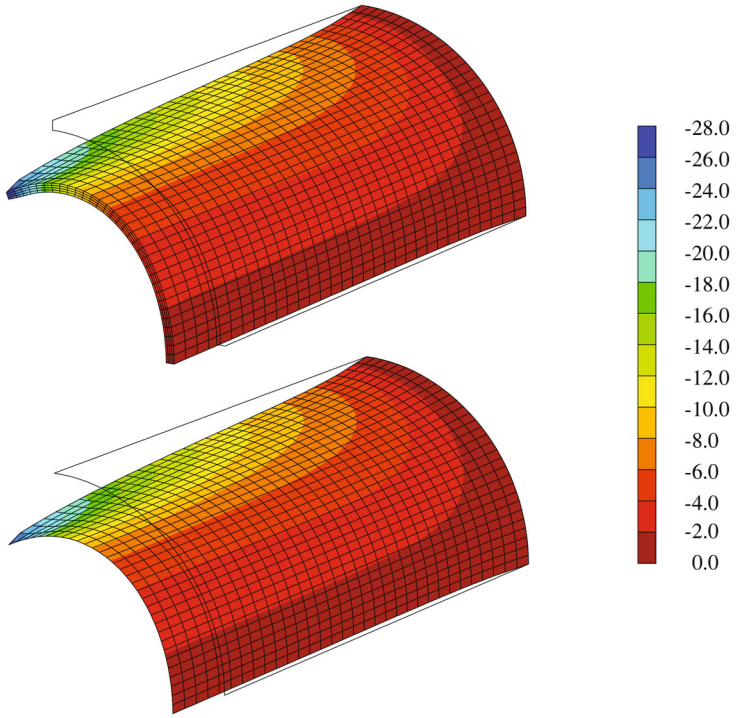

FIGURE 18 Cylindrical shell: displacement u_3 (mm) (above: 3D, below: FE2).

6.6 | Stability analysis of a sandwich plate strip

The sandwich plate strip in Figure 19 is defined in the range $-L/2 \leq x \leq L/2$, $-b/2 \leq y \leq b/2$, and $-h/2 \leq z \leq h/2$, when placing the origin of the $x, y, z-$ coordinate system at the center of the structure.[47,48] The plate consists of a core with thickness t_c and face layers with thickness t_f. The structure is clamped at $x = \pm L/2$. Furthermore, plane strain conditions are assumed in y–direction. The material data for linear isotropic elasticity are E_f, ν_f for the face layers and E_c, ν_c for the core. The plate is loaded by an axial load F. Link conditions ensure the constraint $u_x(L/2, y, z) =$ constant with respect to y and z.

With 100 plate elements in length direction the FE2 solution is converged. The RVE measurements are chosen as $l_x = l_y = h$. It is discretized with one 64-node element for the core and one for each face layer. A 3D reference solution is computed using solid shell element.[42] Hence, in thickness direction 6 elements are used for the core and one element

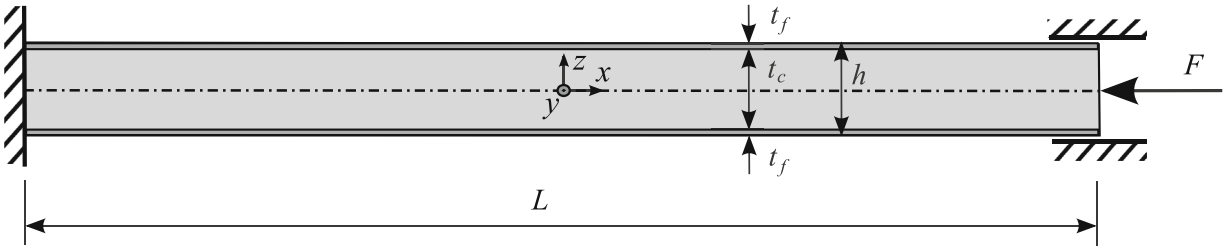

FIGURE 19 Axially loaded sandwich plate strip (not to scale).

for each face layer. In length direction at least 100 elements are necessary to display face layer wrinkling. To allow for antisymmetric buckling modes symmetry conditions are not accounted for. All data are summarized as follows.

Geometrical data		Material data		Meshes	
$L = 800$	mm	$E_f = 70000$	N/mm^2	Plate	$n \times 1$
$b = 60$	mm (width)	$\nu_f = 0.3$		3D	$n \times 1 \times (m+2)$.
$t_c = 30$	mm	E_c	to be varied		$n = 100{,}200$
$t_f = 0.5$	mm	$\nu_c = 0.3$			$m = 6, 10$
$h = 31$	mm				

(61)

As reference value the Euler buckling load

$$F^{\text{Euler}} = \frac{4\,\pi^2\,E_f I_0}{L^2} = 643.181 \text{ kN} \tag{62}$$

with $I_0 = b\,h^3/12$ is computed. Furthermore,

$$F^{\text{shear}} = \frac{E_c\,b\,t_c}{2\,(1+\nu_c)} \tag{63}$$

is defined, which can be derived from a shear buckling mode of the core in the x-z plane. It is a good approximation of the buckling load for $E_c/E_f \ll 1$.[47] In the framework of a linear stability analysis the general eigenvalue problem

$$(\mathbf{K}_L + \Lambda\,\mathbf{K}_{NL})\,\boldsymbol{\Phi} = \mathbf{0} \tag{64}$$

is solved. Here, $\mathbf{K}_L = \mathbf{K}_T(\mathbf{V} = \mathbf{0})$ and $\mathbf{K}_{NL} = \mathbf{K}_T(\mathbf{V}) - \mathbf{K}_L$ are computed with geometrically linear RVEs in dependence of the global displacement vector $\mathbf{V}$. The critical load F^{crit} corresponds to the smallest eigenvalue Λ of the general eigenvalue problem (64). In Figure 20 normalized buckling loads $F^{\text{crit}}/F^{\text{Euler}}$ are plotted in a double logarithmic scale for a variation of the stiffness ratio $10^{-5} \le E_c/E_f \le 1$. As can be seen there is good agreement between the FE2 results and the 3D reference solution. Furthermore, both solutions approach the straight line defined by the critical load F^{shear} for $E_c/E_f \ll 1$.

In Figure 21 buckling modes for three selected ratios E_c/E_f are shown. In the range $10^{-5} \le E_c/E_f \le 10^{-4}$ shear buckling is obtained, whereas for $10^{-4} \le E_c/E_f \le 10^{-3}$ antisymmetric wrinkling of the face layers occurs. In the range $10^{-3} \le E_c/E_f \le 1$ pure Euler buckling is observed. The eigenvectors in Figure 21 are plotted using solid shell element.[42] For the cases a) (shear buckling) and c) (Euler buckling) a $100 \times 1 \times (6+2)$ mesh is used. To capture wrinkling of the face layers in case b) the mesh is refined with $200 \times 1 \times (10+2)$ elements.

6.7 | Inhomogeneous plate strip subjected to a line load

We consider a plate strip with outer dimensions $\ell_x = 360$ cm, $\ell_y = 100$ cm, $h = 8$ cm according to Figure 22. The coordinate system is placed at the center of the plate. At $x = \pm\ell_x/2$ the plate is clamped whereas at the boundaries $y = \pm\ell_y/2$ the displacements u_y are suppressed. Hereby, a constant stress and strain state in y-direction is on hand.

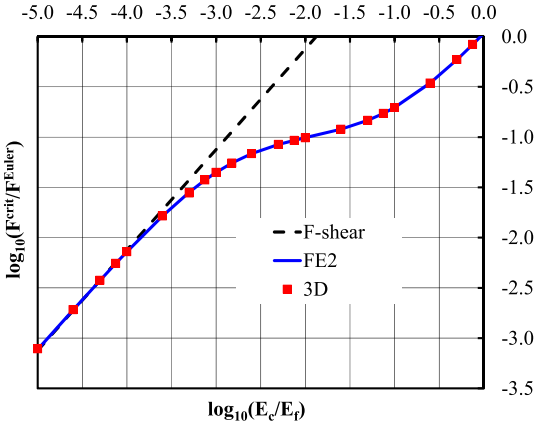

FIGURE 20 Buckling loads of the sandwich plate strip.

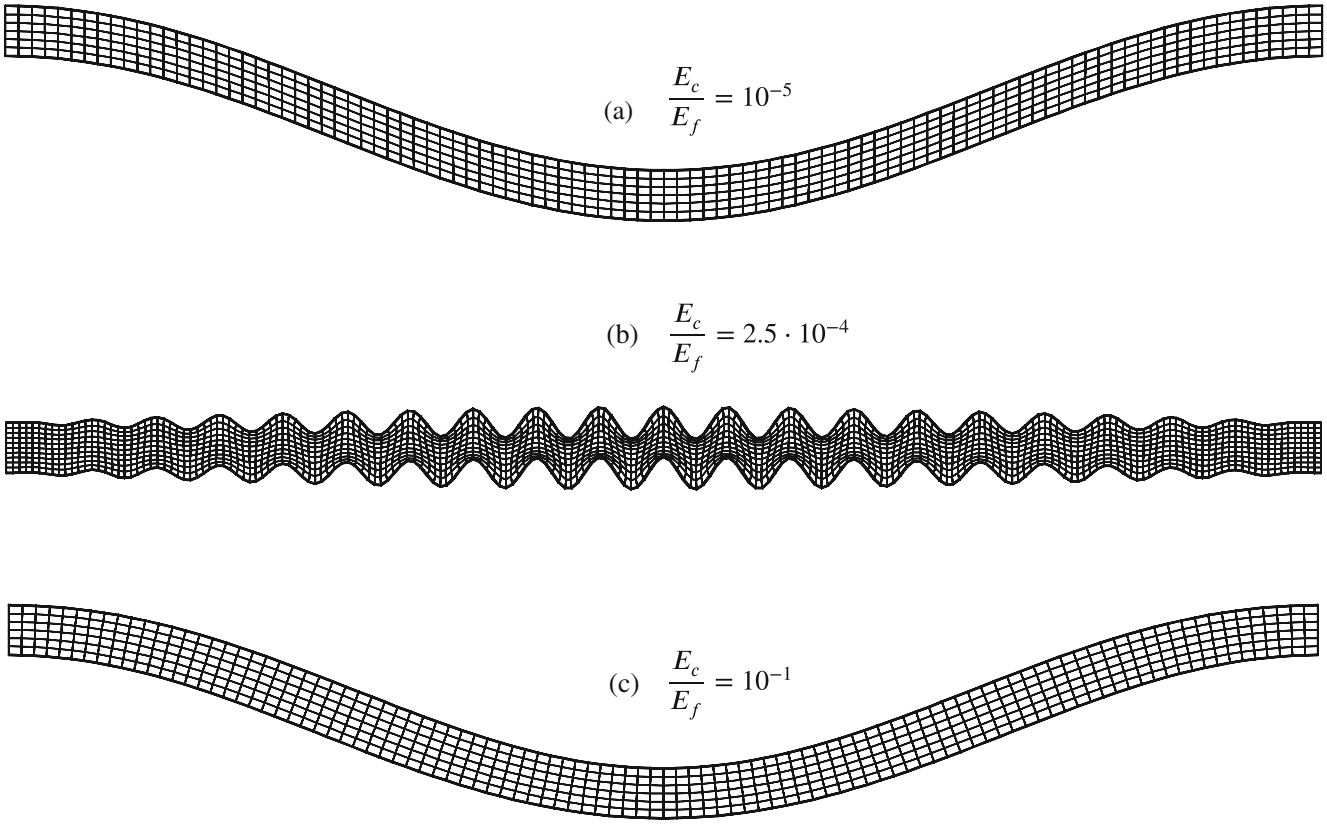

FIGURE 21 Eigenvectors of the sandwich plate strip.

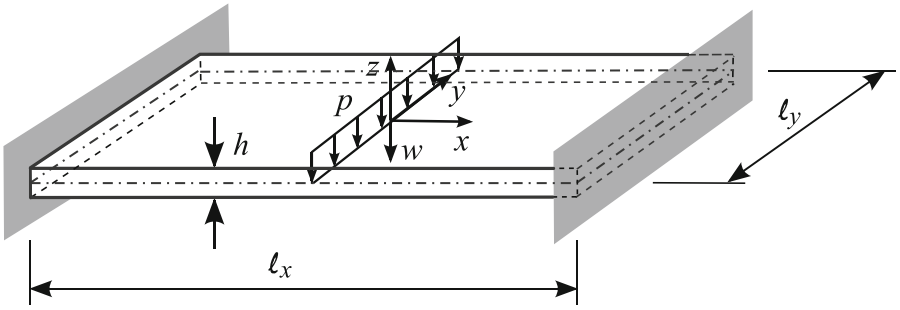

FIGURE 22 Clamped plate strip (not to scale).

The inhomogeneous plate consists of 18 unit cells in x-direction. A unit cell with an inclusion is depicted in Figure 23. The inclusion (in blue) extends through the total width of the plate ℓ_y. The geometrical data are:

$$\begin{aligned} L_x &= 20 \text{ cm}, & L_z &= 8 \text{ cm}, & L_y &= 100 \text{ cm}, \\ L_{x1} &= 4 \text{ cm}, & L_{z1} &= 2 \text{ cm}, & & \\ L_{x2} &= 12 \text{ cm}, & L_{z2} &= 4 \text{ cm}, & & \end{aligned} \tag{65}$$

The geometrical linear computations are performed displacement controlled, thus the constant load p at $x = z = 0$ is obtained as reaction on a prescribed deflection $w = -u_z(x = 0, y, z = 0)$.

We consider isotropic material behavior for the surrounding material (in red) and the inclusion (in blue). The outer material (material 1) is elasto-plastic with Young's modulus E_1, Poisson's ratio ν_1, yield stress y_0 and hardening parameter ξ for linear isotropic hardening. The inclusion material (material 2) is linear elastic with constants E_2 and ν_2. The data are summarized as follows:

$$\begin{aligned} \text{Material 1:} \quad & E_1 = 7000 && \text{kN/cm}^2, \\ & \nu_1 = 0.34, && \\ & y_0 = 12 && \text{kN/cm}^2, \\ & \xi = 100 && \text{kN/cm}^2, \\ \text{Material 2:} \quad & E_2 = 100 && \text{kN/cm}^2, \\ & \nu_2 = 0. && \end{aligned} \tag{66}$$

Considering symmetry of the structure a mesh of 18×1 quadrilateral shell elements is chosen. The RVE consists of one unit cell according to Figure 23. Comparative computations with two or more cells per RVE do not lead to noticeable changes. The discretization is performed with 27–node brick elements. In Figure 23 $n_{x1} = 2$, $n_{x2} = 6$, $n_y = 2$, and $n_{z1} = 2$, $n_{z2} = 4$ denote the number of elements in x-, y-, and z-direction. We compute a 3D reference solution using 27–node brick elements. Considering symmetry only the right half of the structure with 9 cells is discretized. The clamping at $x = \ell_x/2$ is realized with $u_x = u_y = u_z = 0$. Furthermore, the symmetry conditions $u_x(x = 0) = 0$ and $u_y(y = \pm\ell_y/2) = 0$ are enforced. The discretization of a cell corresponds to the discretization of a RVE. Figure 24 shows a view of the 3D mesh in the x-y-plane.

The displacement w is constant in y-direction and is applied in 16 steps with a step size $\Delta w = 0.5$ cm. Subsequently the structure is unloaded. The resultant reaction force $F = p\,\ell_y$ is computed and plotted in Figure 25. There is good agreement between present FE2 solution and the 3D reference solution. Further mesh refinement of the 2D and 3D meshes as well

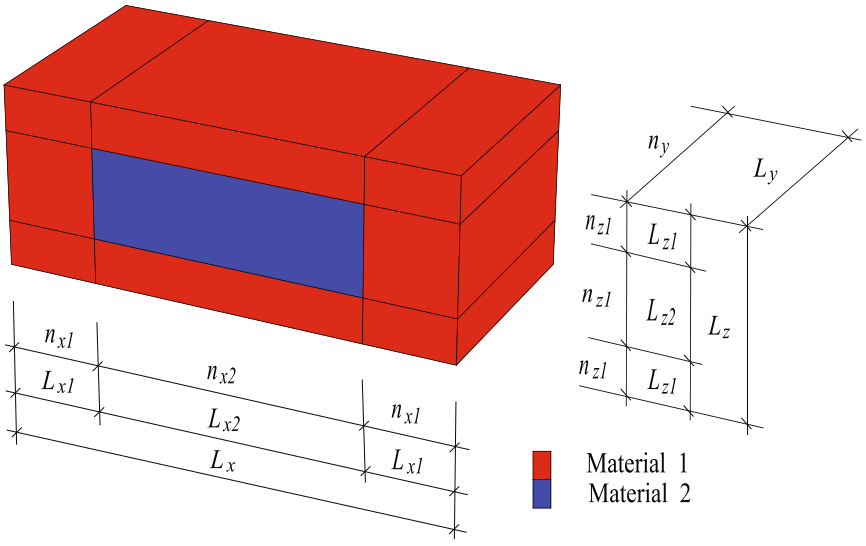

FIGURE 23 Unit cell and RVE: dimensions and discretization data.

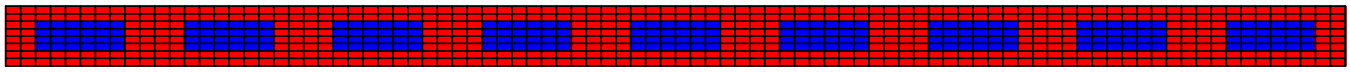

FIGURE 24 View of the 3D mesh in x-z-plane.

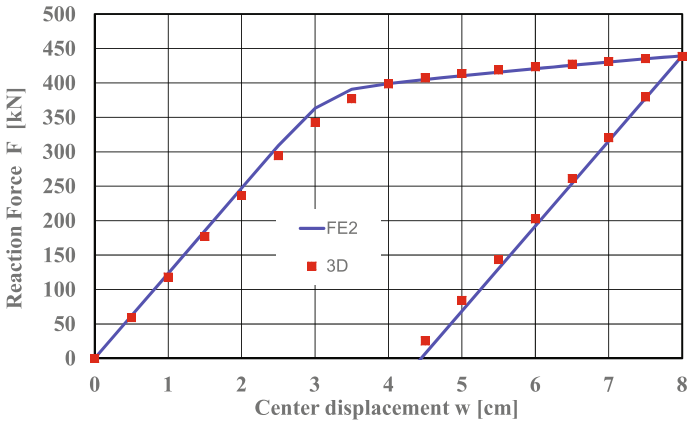

FIGURE 25 Load-deflection curves of the plate strip with inclusions.

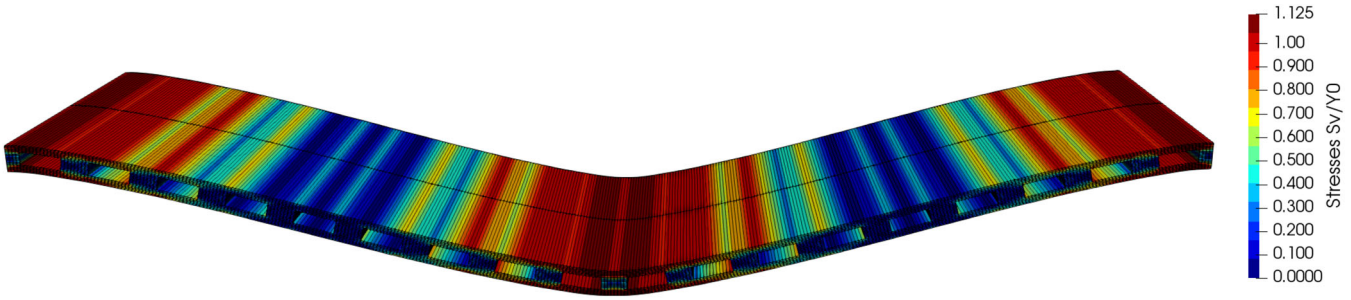

FIGURE 26 Scaled von Mises stresses σ_v/y_0 at $w = 8$ cm.

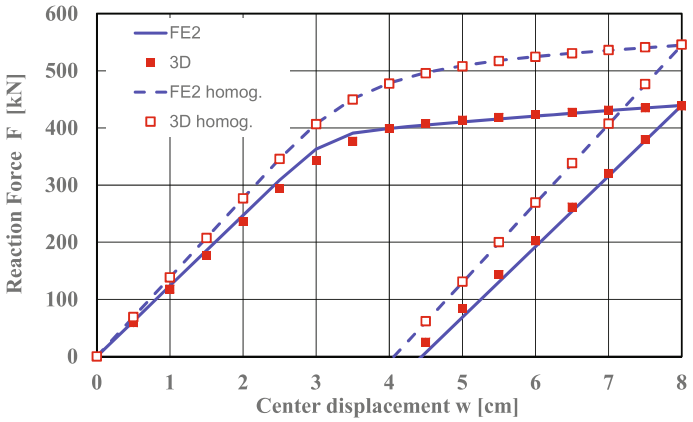

FIGURE 27 Load-deflection curves of the plate strip.

as of the RVE do not lead to noticeable changes. Scaled von Mises stresses σ_v/y_0 of the 3D solution at $w = 8$ cm are shown in Figure 26. The deformations are amplified by a factor 5. The plot shows the complicated stress distribution due to the inclusions.

Finally we analyze the plate strip with a homogeneous composition. Thus the whole plate consists of material 1. Again the two-scale solution is compared with a 3D reference solution computed with 27-noded brick elements. The used meshes correspond to the case with inclusions. Figure 27 proves the good agreement of present FE2 solution with the reference solution. The comparison with the plate with inclusions shows that due to the relative soft inclusion material a considerably different structural response comes out.

7 | CONCLUSIONS

A first order homogenization scheme for Reissner–Mindlin shells that couples the boundary value problems at the coarse and fine scales in a variational setting is presented. Appropriate constraints are developed which prevent both rigid body movements of the RVEs and eliminate the length dependency of the transverse shear stiffness. This is achieved applying the Lagrange multiplier method with 5 or 9 parameters. The version with 5 constraints is recommended as it means the least effort along with the same effect. The periodic boundary conditions for the RVE are applied in such a way that particular membrane, bending and shear modes are not restrained. This is shown by means of a homogeneous RVE, where a material matrix for the stress resultants with decoupled submatrices for membrane, bending and shear is obtained in a correct way. Transformation relations for the stress resultants are applied at the Gauss points of the macro problem and hereby allow the application of the developed FE2 model to finite strain problems. The results of the investigated heterogeneous shells are in very good agreement with 3D reference solutions computed with solid shell elements.

CONFLICT OF INTEREST STATEMENT

The authors declare no potential conflict of interest.

DATA AVAILABILITY STATEMENT

The data that support the findings of this study are available from the corresponding author upon reasonable request.

ACKNOWLEDGMENT

Open Access funding enabled and organized by Projekt DEAL.

ORCID

Friedrich Gruttmann https://orcid.org/0000-0001-7274-869X
Werner Wagner https://orcid.org/0000-0001-5809-4538

REFERENCES

1. Zohdi TI, Wriggers P. *Introduction to Computational Micromechanics*. Springer Series: Lecture Notes in Applied and Computational Mechanics. Vol 20. Springer; 2005.
2. De Borst R, Ramm E. *Multiscale Methods in Computational Mechanics: Progress And Accomplishments*. Springer Series: Lecture Notes in Applied and Computational Mechanics. Vol 55. Springer; 2011.
3. Guedes JM, Kikuchi N. Preprocessing and postprocessing for materials based on the homogenization method with adaptive finite element methods. *Comput Methods Appl Mech Eng*. 1990;83:143-198.
4. Ghosh S, Lee K, Moorthy S. Two scale analysis of heterogeneous elastic-plastic materials with asymptotic homogenisation and Voronoi cell finite element model. *Comput Methods Appl Mech Eng*. 1996;132:63-116.
5. Michel JC, Moulinec H, Suquet P. Effective properties of composite materials with periodic microstructure: a computational approach. *Comput Methods Appl Mech Eng*. 1999;172:109-143.
6. Miehe C, Schröder J, Schotte J. Computational homogenization analysis in finite plasticity, simulation of texture development in polycrystalline materials. *Comput Methods Appl Mech Eng*. 1999;171:387-418.
7. Feyel F, Chaboche JL. FE2 multiscale approach for modelling the elastoviscoplastic behavior of long fiber SiC/Ti composite materials. *Comput Methods Appl Mech Eng*. 2000;183:309-330.
8. Terada K, Kikuchi N. A class of general algorithms for multi-scale analysis of heterogeneous media. *Comput Methods Appl Mech Eng*. 2001;190:5427-5464.
9. Miehe C. Strain-driven homogenization of inelastic microstructures and composites based on an incremental variational formulation. *Int J Numer Methods Eng*. 2002;55:1285-1322.

10. Moyeda A, Fish J. Multiscale analysis of solid, waffle, ribbed and hollowcore reinforced concrete slabs. *Comput Methods Appl Mech Eng*. 2019;348:139-156.
11. Hohe J, Becker W. Effective stress–strain relations for two dimensional cellular sandwich cores: homogenization, material models, and properties. *Appl Mech Rev*. 2002;55:61-87.
12. Rabczuk T, Kim JY, Samaniego E, Belytschko T. Homogenization of sandwich structures. *Int J Numer Methods Eng*. 2004;61:1009-1027.
13. Liu T, Deng ZC, Lu TJ. Design optimization of truss-cored sandwiches with homogenization. *Int J Solids Struct*. 2006;43:7891-7918.
14. Gigliotti L, Pinho ST. Exploiting symmetries in solid-to-shell homogenization, with application to periodic pin-reinforced sandwich structures. *Compos Struct*. 2015;132:995-1005.
15. Cecchi A, Sab K. Out-of-plane model for heterogeneous periodic materials: the case of masonry. *Eur J Mech A Solids*. 2002;21:715-746.
16. Cecchi A, Milani G, Tralli A. A Reissner-Mindlin limit analysis model for out-of-plane loaded running bond masonry walls. *Int J Solids Struct*. 2007;44:1438-1460.
17. Mercatoris BCN, Bouillard P, Massart TJ. Multi-scale detection of failure in planar masonry thin shells using computational homogenization. *Eng Fract Mech*. 2009;76:479-499.
18. Mercatoris BCN, Massart TJ. A coupled two–scale computational scheme for the failure of periodic quasi-brittle thin planar shells and its application to masonry. *Int J Numer Methods Eng*. 2011;85:1177-1206.
19. Kouznetsova VG, Geers MGD, Brekelmans WAM. Multi-scale second-order computational homogenization of multi-phase materials: A nested finite element solution strategy. *Comput Methods Appl Mech Eng*. 2004;193:5525-5550.
20. Geers MGD, Coenen EWC, Kouznetsova VG. Multi–scale computational homogenization of structured thin sheets. *Model Simul Mater Sci Eng*. 2007;15:S393-S404.
21. Coenen EWC, Kouznetsova VG, Geers MGD. Computational homogenization for heterogeneous thin sheets. *Int J Numer Methods Eng*. 2010;83:1180-1205.
22. Luscher D, McDowell D, Bronkhorst C. Essential features of fine scale boundary conditions for second gradient multiscale homogenization of statistical volume elements. *Int J Multiscale Comput Eng*. 2012;10(5):461-486.
23. Helfen C, Diebels S. A numerical homogenisation method for sandwich plates based on a plate theory with thickness change. *Z Angew Math Mech*. 2013;93(2-3):113-125.
24. Larsson R, Landervik M. A stress-resultant shell theory based on multiscale homogenization. *Comput Methods Appl Mech Eng*. 2013;263:1-11.
25. Gruttmann F, Wagner W. A coupled two-scale shell model with applications to layered structures. *Int J Numer Methods Eng*. 2013;94:1233-1254.
26. Heller D, Gruttmann F. Nonlinear two-scale shell modeling of sandwiches with a comb-like core. *Compos Struct*. 2016;144:147-155.
27. Cong Y, Nezamabadi S, Zahrouni H, Yvonnet J. Multiscale computational homogenization of heterogeneous shells at small strains with extensions to finite displacement and buckling. *Int J Numer Methods Eng*. 2015;104:235-259.
28. Främby J, Brouzoulis J, Fagerström M. Assessment of two methods for the accurate prediction of transverse stress distributions in laminates. *Compos Struct*. 2016;140:602-611.
29. Klarmann S, Gruttmann F, Klinkel S. Homogenization assumptions for coupled multiscale analysis of structural elements: beam kinematics. *Comput Mech*. 2020;65:635-661.
30. Hii AKW, El Said B. A kinematically consistent second-order computational homogenisation framework for thick shell models. *Comput Methods Appl Mech Eng*. 2022;398:115136.
31. Sotiropoulos G, Papadopoulos V. Nonlinear multiscale modeling of thin composite shells at finite deformations. *Comput Methods Appl Mech Eng*. 2022;391:114572.
32. Müller M, Klarmann S, Gruttmann F. A new homogenization scheme for beam and plate structures without a priori requirements on boundary conditions. *Comput Mech*. 2022;70(6):1167-1187.
33. Zhi J, Leong KH, Yeoh KM, Tay TE, Tan VBC. Multiscale modeling of laminated thin-shell structures with Direct FE2. *Comput Methods Appl Mech Eng*. 2023;407:115942.
34. Turon F, Otero F, Martinez X. Multi-scale procedure for the mechanical analysis of composite laminate structures considering mixed boundary conditions. *Compos Struct*. 2023;322:117343.
35. Börjesson E, Larsson F, Runesson K, Remmers JJC, Fagerström M. Variationally consistent homogenisation of plates. *Comput Methods Appl Mech Eng*. 2023;413:116094.
36. Mester L, Klarmann S, Klinkel S. Homogenization assumptions for the two-scale analysis of first-order shear deformable shells. *Comput Mech*. 2023. doi:10.1007/s00466-023-02390-z
37. Wagner W, Gruttmann F. A robust nonlinear mixed hybrid quadrilateral shell element. *Int J Numer Methods Eng*. 2005;64:635-666.
38. Hill R. Elastic properties of reinforced solids: some theoretical principles. *J Mech Phys Solids*. 1963;11:357-372.
39. Gruttmann F, Wagner W. Structural analysis of composite laminates using a mixed hybrid shell element. *Comput Mech*. 2006;37:479-497.
40. Dvorkin E, Bathe KJ. A continuum mechanics based four node shell element for general nonlinear analysis. *Eng Comput*. 1984;1:77-88.
41. Taylor RL. FEAP. http://www.ce.berkeley.edu/projects/feap/ 2023.
42. Klinkel S, Gruttmann F, Wagner W. A continuum based 3D–shell element for laminated structures. *Comput Struct*. 1999;71:43-62.
43. Klinkel S, Gruttmann F, Wagner W. A robust non–linear solid shell element based on a mixed variational formulation. *Comput Methods Appl Mech Eng*. 2006;195:179-201.
44. Reissner E. On bending of elastic plates. *Q Appl Math*. 1947;5:55-68.
45. Vlachoutsis S. Shear correction factors for plates and shells. *Int J Numer Methods Eng*. 1992;33(7):1537-1552.

46. Gruttmann F, Wagner W. Shear correction factors for layered plates and shells. *Comput Mech*. 2017;59:129-146.
47. Rammerstorfer FG, Dorninger K, Starlinger A. Nonlinear finite element analysis of composite and sandwich shell structures. In: Wriggers P, Wagner W, eds. *Nonlinear Computational Mechanics, State of the Art*. Springer Berlin; 1991:332-359.
48. Gruttmann F, Knust G, Wagner W. Theory and numerics of layered shells with variationally embedded interlaminar stresses. *Comput Methods Appl Mech Eng*. 2017;326:713-738.
49. Doyle TC, Ericksen JL. Non-linear Elasticity. *Adv Appl Mech*. 1956;4:53-115.
50. Seth BR. Generalized strain measure with application to physical problems. In: Rainer M, Abir D, eds. *Second–Order Effects in Elasticity, Plasticity and Fluid Dynamics*. Pergamon Press; 1964:162-172.
51. Hill R. Aspects of invariance in solid mechanics. *Adv Appl Mech*. 1978;18:1-75.
52. Schröder J, Gruttmann F, Löblein J. A simple orthotropic finite elasto–plasticity model based on generalized stress–strain measures. *Comput Mech*. 2002;30:48-64.
53. Ogden RW. *Non–Linear Elastic Deformations*. Ellis Horwood; 1984.

How to cite this article: Gruttmann F, Wagner W. A FE2 shell model with periodic boundary conditions for thin and thick shells. *Int J Numer Methods Eng*. 2024;125(11):e7433. doi: 10.1002/nme.7433

APPENDIX. A VARIATION AND LINEARIZATION OF GENERALIZED STRAIN MEASURES

To alleviate the notation the overbar which indicates averaged quantities of the macro problem is omitted in this appendix. Following for example, Doyle and Ericksen,[49] Seth[50] or Hill[51] generalized strain measures are defined as

$$\mathbf{E}^{(k)} := \begin{cases} \dfrac{1}{2\,k}(\mathbf{C}^k - \mathbf{1}) & \text{for } k \neq 0, \\ \dfrac{1}{2}\ \ln[\mathbf{C}] & \text{for } k = 0. \end{cases} \tag{A1}$$

Here $\mathbf{C} = \mathbf{F}^T\,\mathbf{F}$ and $\mathbf{1}$ denote the right Cauchy–Green tensor and the second-order unit tensor, respectively. The Green–Lagrange strain tensor $\mathbf{E} = \mathbf{E}^{(1)} = \frac{1}{2}(\mathbf{C} - \mathbf{1})$ is contained as special case. In the following we consider only the case $k \neq 0$, as we are interested to compute the right stretch tensor $\mathbf{U} = \mathbf{C}^k$ with $k = 1/2$.

Let $\lambda_A, A = 1, 2, 3$ be the eigenvalues and $\mathbf{N}^A$ the eigenvectors of $\mathbf{C} = 2\,\mathbf{E} + \mathbf{1}$ one obtains

$$\mathbf{E}^{(k)} = \sum_{A=1}^{3} E_A^{(k)}\ \mathbf{N}^A \otimes \mathbf{N}^A = E_{ij}^{(k)}\ \mathbf{e}_i \otimes \mathbf{e}_j \tag{A2}$$

with $E_A^{(k)} = \frac{1}{2\,k}(\lambda_A^k - 1)$ and the Cartesian basis $\mathbf{e}_i$.

Hereinafter we apply Voigt notation, thus

$$\mathbf{E}^{(k)} = \left[E_{11}^{(k)},\ E_{22}^{(k)},\ E_{33}^{(k)},\ 2\,E_{12}^{(k)},\ 2\,E_{13}^{(k)},\ 2\,E_{23}^{(k)}\right]^T. \tag{A3}$$

The vector of generalized stresses $\mathbf{S}^{(k)}$ is work conjugate to $\mathbf{E}^{(k)}$. In order to derive the transformation relations between the Second Piola–Kirchhoff stresses $\mathbf{S} = \mathbf{S}^{(1)}$ and $\mathbf{S}^{(k)}$ as well as the associated moduli we insert $\delta\mathbf{E}^{(k)} = \mathbb{P}\ \delta\mathbf{E}$ and $\Delta\mathbf{E}^{(k)} = \mathbb{P}\ \Delta\mathbf{E}$ with $\mathbb{P} = \partial_{\mathbf{E}}\mathbf{E}^{(k)}$ as well as $\Delta\delta\mathbf{E}^{(k)T}\mathbf{S}^{(k)} = \delta\mathbf{E}^T\ \mathbb{L}\ \Delta\mathbf{E}$ into the linearized virtual work per unit volume

$$\begin{aligned} \delta\mathbf{E}^{(k)T}\mathbf{S}^{(k)} + \Delta(\delta\mathbf{E}^{(k)T}\mathbf{S}^{(k)}) &= \delta\mathbf{E}^{(k)T}(\mathbf{S}^{(k)} + \mathbb{C}^{(k)}\ \Delta\mathbf{E}) + \Delta\delta\mathbf{E}^{(m)T}\mathbf{S}^{(k)} \\ &= \delta\mathbf{E}^T[\mathbb{P}^T\ \mathbf{S}^{(k)} + (\mathbb{P}^T\ \mathbb{C}^{(k)}\ \mathbb{P} + \mathbb{L})\ \Delta\mathbf{E}]. \end{aligned} \tag{A4}$$

From Equation (A4) the transformations $\mathbf{S} = \mathbb{P}^T\ \mathbf{S}^{(k)}$ and associated moduli $\mathbb{C} = \mathbb{P}^T\ \mathbb{C}^{(k)}\ \mathbb{P} + \mathbb{L}$ with $\mathbb{C}^{(k)} = \partial_{\mathbf{E}^{(k)}}\mathbf{S}^{(k)}$ can be deduced.

Explicit component representations of the matrices $\mathbb{P}$ and $\mathbb{L}$ have been derived in Schröder et al.[52] exploiting results of Ogden.[53] Now following Reference 52 the symmetric matrix $\hat{\mathbb{P}} = \mathbf{T}^T\mathbf{L}_1\mathbf{T}$ is introduced, where $\mathbf{T}$ is computed with the

eigenvector components $N_j^A = \mathbf{N}^A \cdot \mathbf{e}_j$

$$\mathbf{T} = \begin{bmatrix} (N_1^1)^2 & (N_2^1)^2 & (N_3^1)^2 & N_1^1 N_2^1 & N_1^1 N_3^1 & N_2^1 N_3^1 \\ (N_1^2)^2 & (N_2^2)^2 & (N_3^2)^2 & N_1^2 N_2^2 & N_1^2 N_3^2 & N_2^2 N_3^2 \\ (N_1^3)^2 & (N_2^3)^2 & (N_3^3)^2 & N_1^3 N_2^3 & N_1^3 N_3^3 & N_2^3 N_3^3 \\ 2N_1^1 N_1^2 & 2N_2^1 N_2^2 & 2N_3^1 N_3^2 & N_1^1 N_2^2 + N_2^1 N_1^2 & N_1^1 N_3^2 + N_3^1 N_1^2 & N_2^1 N_3^2 + N_3^1 N_2^2 \\ 2N_1^1 N_1^3 & 2N_2^1 N_2^3 & 2N_3^1 N_3^3 & N_1^1 N_2^3 + N_2^1 N_1^3 & N_1^1 N_3^3 + N_3^1 N_1^3 & N_2^1 N_3^3 + N_3^1 N_2^3 \\ 2N_1^2 N_1^3 & 2N_2^2 N_2^3 & 2N_3^2 N_3^3 & N_1^2 N_2^3 + N_2^2 N_1^3 & N_1^2 N_3^3 + N_3^2 N_1^3 & N_2^2 N_3^3 + N_3^2 N_2^3 \end{bmatrix}. \tag{A5}$$

The diagonal matrix $\mathbf{L}_1$ reads

$$\begin{aligned} \mathbf{L}_1 &= \operatorname{diag}\left[\lambda_1^{k-1}, \quad \lambda_2^{k-1}, \quad \lambda_3^{k-1}, \quad \gamma_{12}^{(k)}, \quad \gamma_{13}^{(k)}, \quad \gamma_{23}^{(k)}\right], \\ \gamma_{AB}^{(k)} &= \begin{cases} \dfrac{E_A^{(k)} - E_B^{(k)}}{\lambda_A - \lambda_B} & \text{for} \quad \lambda_A \neq \lambda_B, \\ \dfrac{1}{2}\lambda_A^{k-1} & \text{for} \quad \lambda_A = \lambda_B. \end{cases} \end{aligned} \tag{A6}$$

Now the component representation of $\mathbb{P}$ is given as

$$\mathbb{P} = \begin{bmatrix} P_{11} & P_{12} & P_{13} & P_{14} & P_{15} & P_{16} \\ P_{21} & P_{22} & P_{23} & P_{24} & P_{25} & P_{26} \\ P_{31} & P_{32} & P_{33} & P_{34} & P_{35} & P_{36} \\ P_{41} & P_{42} & P_{43} & P_{44} & P_{45} & P_{46} \\ P_{51} & P_{52} & P_{53} & P_{54} & P_{55} & P_{56} \\ P_{61} & P_{62} & P_{63} & P_{64} & P_{65} & P_{66} \end{bmatrix} = \begin{bmatrix} \hat{P}_{11} & \hat{P}_{12} & \hat{P}_{13} & \hat{P}_{14} & \hat{P}_{15} & \hat{P}_{16} \\ \hat{P}_{21} & \hat{P}_{22} & \hat{P}_{23} & \hat{P}_{24} & \hat{P}_{25} & \hat{P}_{26} \\ \hat{P}_{31} & \hat{P}_{32} & \hat{P}_{33} & \hat{P}_{34} & \hat{P}_{35} & \hat{P}_{36} \\ 2\,\hat{P}_{41} & 2\,\hat{P}_{42} & 2\,\hat{P}_{43} & 2\,\hat{P}_{44} & 2\,\hat{P}_{45} & 2\,\hat{P}_{46} \\ 2\,\hat{P}_{51} & 2\,\hat{P}_{52} & 2\,\hat{P}_{53} & 2\,\hat{P}_{54} & 2\,\hat{P}_{55} & 2\,\hat{P}_{56} \\ 2\,\hat{P}_{61} & 2\,\hat{P}_{62} & 2\,\hat{P}_{63} & 2\,\hat{P}_{64} & 2\,\hat{P}_{65} & 2\,P_{66} \end{bmatrix}, \tag{A7}$$

where $\hat{P}_{ij}$ are components of $\hat{\mathbb{P}} = \mathbf{T}^T \mathbf{L}_1 \mathbf{T}$. In Reference 52 the factor 2 is assigned to the shear terms of $\mathbf{S}^{(k)}$ and $\mathbb{C}^{(k)}$, however in present case the represented version of $\mathbb{P}$ is better suited.

The matrix representation of the product term $\Delta\delta\mathbf{E}^{(k)T}\,\mathbf{S}^{(k)} = \delta\mathbf{E}^T\,\mathbb{L}\,\Delta\mathbf{E}$ reads

$$\Delta\delta\mathbf{E}^{(k)T}\,\mathbf{S}^{(k)} = \begin{bmatrix} \delta E_{11} \\ \delta E_{22} \\ \delta E_{33} \\ 2\delta E_{12} \\ 2\delta E_{13} \\ 2\delta E_{23} \end{bmatrix}^T \begin{bmatrix} L_{11} & L_{12} & L_{13} & L_{14} & L_{15} & L_{15} \\ L_{21} & L_{22} & L_{23} & L_{24} & L_{25} & L_{26} \\ L_{31} & L_{32} & L_{33} & L_{34} & L_{35} & L_{36} \\ L_{41} & L_{42} & L_{43} & L_{44} & L_{45} & L_{46} \\ L_{51} & L_{52} & L_{53} & L_{54} & L_{55} & L_{56} \\ L_{61} & L_{62} & L_{63} & L_{64} & L_{65} & L_{66} \end{bmatrix} \begin{bmatrix} \Delta E_{11} \\ \Delta E_{22} \\ \Delta E_{33} \\ 2\Delta E_{12} \\ 2\Delta E_{13} \\ 2\Delta E_{23} \end{bmatrix}, \tag{A8}$$

where $L_{ij} = L_{ji}$ are components of $\mathbb{L} = \mathbf{T}^T\,\mathbf{L}_2\,\mathbf{T}$ with the symmetric matrix

$$\mathbf{L}_2 = \begin{bmatrix} L_{1111} & 0 & 0 & L_{1112} & L_{1113} & 0 \\ & L_{2222} & 0 & L_{2212} & 0 & L_{2223} \\ & & L_{3333} & 0 & L_{3313} & L_{3323} \\ & & & L_{1212} & L_{1213} & L_{1223} \\ & \text{sym.} & & & L_{1313} & L_{1323} \\ & & & & & L_{2323} \end{bmatrix}. \tag{A9}$$

In case of $\lambda_1 \neq \lambda_2 \neq \lambda_3$ the non vanishing components read

$$
\begin{aligned}
L_{1111} &= 2\, S_{11}^{(k)}(k-1)\, \lambda_1^{k-2},\\
L_{2222} &= 2\, S_{22}^{(k)}(k-1)\, \lambda_2^{k-2},\\
L_{3333} &= 2\, S_{33}^{(k)}(k-1)\, \lambda_3^{k-2},\\
L_{1212} &= S_{11}^{(k)}\, \gamma_{112}^{(k)} + S_{22}^{(k)}\, \gamma_{221}^{(k)},\\
L_{1313} &= S_{11}^{(k)}\, \gamma_{113}^{(k)} + S_{33}^{(k)}\, \gamma_{331}^{(k)},\\
L_{2323} &= S_{22}^{(k)}\, \gamma_{223}^{(k)} + S_{33}^{(m)}\, \gamma_{332}^{(k)},\\
L_{1112} &= 2\, S_{12}^{(k)}\, \gamma_{112}^{(k)},\\
L_{2212} &= 2\, S_{12}^{(k)}\, \gamma_{221}^{(k)},\\
L_{1113} &= 2\, S_{13}^{(k)}\, \gamma_{113}^{(k)},\\
L_{3313} &= 2\, S_{13}^{(k)}\, \gamma_{331}^{(k)},\\
L_{2223} &= 2\, S_{23}^{(k)}\, \gamma_{223}^{(k)},\\
L_{3323} &= 2\, S_{23}^{(k)}\, \gamma_{332}^{(k)},\\
L_{1223} &= 2\, S_{13}^{(k)}\, \gamma^{(k)},\\
L_{1323} &= 2\, S_{12}^{(k)}\, \gamma^{(k)},\\
L_{1213} &= 2\, S_{23}^{(k)}\, \gamma^{(k)},
\end{aligned}
\tag{A10}
$$

with

$$
\begin{aligned}
\gamma_{AAB}^{(k)} &= \frac{\lambda_A^{k-1}(\lambda_A - \lambda_B) - 2(E_A^{(k)} - E_B^{(k)})}{(\lambda_A - \lambda_B)^2}\\
\gamma^{(k)} &= \frac{\lambda_1(E_2^{(k)} - E_3^{(k)}) + \lambda_2(E_3^{(k)} - E_1^{(k)}) + \lambda_3(E_1^{(k)} - E_2^{(k)})}{(\lambda_1 - \lambda_2)(\lambda_2 - \lambda_3)(\lambda_3 - \lambda_1)}.
\end{aligned}
\tag{A11}
$$

The components $S_{AB}^{(k)}$ of the generalized stress tensor with respect to the eigenvector basis $\mathbf{N}^A$ are evaluated as

$$
\begin{aligned}
\hat{\mathbf{S}} &= \mathbf{T}\, \bar{\mathbf{S}},\\
\hat{\mathbf{S}} &= \left[S_{11}^{(k)}, S_{22}^{(k)}, S_{33}^{(k)}, 2S_{12}^{(k)}, 2S_{13}^{(k)}, 2S_{23}^{(k)}\right]^T,\\
\bar{\mathbf{S}} &= \left[\bar{S}_{11}, \bar{S}_{22}, \bar{S}_{33}, 2\bar{S}_{12}, 2\bar{S}_{13}, 2\bar{S}_{23}\right]^T,
\end{aligned}
\tag{A12}
$$

where $\bar{S}_{ij}$ are the Cartesian components of the generalized stress tensor. For isotropic material behavior and $A \neq B$ it holds $S_{AB}^{(k)} = 0$.

For the cases of two or three equal eigenvalues we refer to the representation of $\mathbf{L}_2$ in appendix B of Reference 52. The alternative is the prevention of equal eigenvalues by a small perturbation.